https://doi.org/10.5194/wes-2026-149
Preprint. Discussion started: 27 August 2026

eawe european academy of wind energy
Open Access WIND ENERGY SCIENCE DISCUSSIONS

The TANDEM wake model: coupled turbulence and deficit momentum modeling in stratified atmospheric boundary layers

Kirby S. Heck[1] and Michael F. Howland[1]

[1]Civil and Environmental Engineering, Massachusetts Institute of Technology, Cambridge, MA 02139, USA

Correspondence: Michael F. Howland (mhowland@mit.edu)

Abstract. Engineering wake models are essential tools for estimating aerodynamic interactions between wind turbines. All utility-scale wind turbines operate in the atmospheric boundary layer (ABL), where Coriolis forces and stratification shape the structure and dynamics of wake evolution, but these effects are often neglected or highly simplified in engineering wake models. We propose the TANDEM (Turbulence ANd DEficit Momentum) framework in which the wake deficit is computed by co-evolving a parabolized equation for the streamwise momentum deficit jointly with a parabolized equation for the wake-added turbulence kinetic energy (TKE) using a one-equation eddy viscosity closure. The eddy viscosity formulation uses a generalized mixing length, which interpolates Monin–Obukhov similarity theory in the surface layer and a dynamics-dependent wake mixing length above the surface layer. The TANDEM wake model is coupled with an initial condition from the Unified Momentum Model, which generalizes classical theory to include turbine yaw misalignment and high thrust coefficients. Single-turbine wake predictions using the TANDEM wake model capture the skewed wake shape and enhanced wake recovery in veered conditions that are coarsely parameterized or neglected by existing analytical models, when compared with large-eddy simulations (LES). Across neutrally and stably stratified ABLs, the TANDEM model predicts normalized downstream power production of a single turbine with a mean absolute error (MAE) of 4.3%, compared with 6.5% for a skewed Gaussian model or 21% for an axisymmetric Gaussian model. In a four-turbine wind farm, the TANDEM model provides the lowest predictive error of farm power among the tested models across full- and partial-wake conditions. Further, the MAE of normalized turbine power predictions in a 25-turbine wake steering case study is 4.7% for the TANDEM model, compared with 8.8% for an analytical vortex sheet model and 11% for a Gaussian wake model. Continued work on coupling array-scale effects with turbine-scale wake evolution is recommended to improve TANDEM model predictions in moderate to large wind farms. Nonetheless, we see the TANDEM framework as a promising scaffold to build a new class of wake models for improved wake predictions in ABL flows.

1 Introduction

Mitigating wake interactions within wind turbine arrays relies on understanding how momentum and energy are replenished into the wake region through turbulent mixing. Utility-scale wind turbines extract power from the atmospheric boundary layer (ABL) (Stevens and Meneveau, 2017), where wake transport mechanisms are affected by processes including wind shear and wind veer, vertical gradients of wind speed and wind direction, respectively (Abkar and Porté-Agel, 2016; Bromm et al., 2017),

https://doi.org/10.5194/wes-2026-149
Preprint. Discussion started: 27 August 2026

turbulence (Wu and Porté-Agel, 2012; Gambuzza and Ganapathisubramani, 2023), stratification (Chamorro and Porté-Agel, 2010; Xie and Archer, 2017; Du et al., 2021), and Coriolis forcing (van der Laan and Sørensen, 2017; Howland et al., 2020; Heck and Howland, 2025). These processes affect the flow dynamics and rate of wake recovery and alter the structure of the wake (e.g. Abkar and Porté-Agel, 2016; Klemmer and Howland, 2024). However, resolving and modeling the interactions between the wind turbine wakes and the ABL often requires expensive numerical simulations, such as computational fluid dynamics (Porté-Agel et al., 2020; van der Laan et al., 2024; Heck and Howland, 2026), which are not practical for wind energy engineering applications, such as wind farm siting and control optimization (Meyers et al., 2022).

In contrast to the richness and high-dimensionality of ABL physics, most wind turbine wake models are designed for neutrally stratified flow in the ABL surface layer and neglect Coriolis effects (Jensen, 1983; Frandsen et al., 2006; Bastankhah and Porté-Agel, 2014, 2016). All wake models use physics-based and/or heuristic simplifications to reduce the turbulent flow physics to an analytical or efficient numerical form. However, these assumptions often neglect key transport processes between the wake and ABL, despite the significant body of literature noting the importance of ABL physics on wind farm aerodynamics.

To begin to bridge the gap between ABL physics and wake modeling, recent studies have proposed new models specifically developed for wakes in the stratified ABL. These include extensions to analytical wake models to account for the asymmetric wake expansion in stratification (Abkar and Porté-Agel, 2015), wake elongation in veered inflows (Abkar et al., 2018; Narasimhan et al., 2022; Mohammadi et al., 2022; Narasimhan et al., 2025), and effects of yaw-misalignment with the incident flow (Bastankhah and Porté-Agel, 2016; Shapiro et al., 2020; Bastankhah et al., 2022), which is ubiquitous in the ABL. In parallel, numerical wake modeling offers an alternative approach, often with increased model flexibility, to incorporate additional flow processes into a wake model. For example, Martínez-Tossas et al. (2021) derived a prognostic, parabolic partial differential equation (PDE) for the streamwise wake evolution in the ABL using a novel flow double-decomposition. This so-called curled wake model, which builds on previous parabolized approaches to numerical wake modeling (Ainslie, 1988; Iungo et al., 2018; Martínez-Tossas et al., 2019), captures wind veer and wall effects by computing the advection and turbulence terms.

Separately, wind turbine wakes also induce mixing and elevate levels of turbulence kinetic energy (TKE) downstream. The excess TKE in the wake, or wake-added TKE, has been a smaller focus of the wake modeling community, where models are often highly empirical and calibrated to data in neutrally stratified flows (c.f. Crespo and Hernández, 1996). Instead, it is often assumed that the wake evolution only depends on the TKE (or equivalently, turbulence intensity, TI) incident to the turbine generating the wake (Peña et al., 2016; Niayifar and Porté-Agel, 2016; Shapiro et al., 2020; Bastankhah et al., 2022). Rarely are the wake velocity deficit and wake-added turbulence coupled together. Rather, the wake-added TKE is either predicted solely by the inflow properties and turbine operation (e.g. Crespo and Hernández, 1996; Qian and Ishihara, 2018) or additionally based on a prescribed wake velocity profile (Bastankhah et al., 2024). An exception is the TurbOPark wake model (Pedersen et al., 2022), which analytically integrates a wake-added TI model to derive an analytical, non-linear wake spreading rate that varies with the distance downstream of the turbine. Despite this, the coupled nature of the wake velocity and wake-added TKE has been largely unexplored by the wake modeling community.

Nonetheless, wake velocity and wake-added TKE are inextricably linked. For example, stronger wakes (larger magnitude of wake velocity deficit) create stronger shear, thereby producing more wake-added TKE, and recover more rapidly than weaker wakes (Martínez-Tossas et al., 2022; Heck et al., 2024). Other studies have found that despite the buoyant destruction of turbulence in the stably stratified boundary layer (SBL), the wake-added TKE can be higher in the SBL than in neutral ABLs (Klemmer and Howland, 2024; Wu et al., 2024). Furthermore, Klemmer and Howland (2024) showed through a budget analysis that the increase in wake-added TKE can be attributed to the enhanced shear production in the SBL. Leveraging these insights, Klemmer and Howland (2025) proposed a wake model that coupled a parabolized wake-added TKE equation with the streamwise momentum deficit equation to yield simultaneous predictions of wake velocities and added turbulence.

In this study, we introduce the Turbulence ANd DEficit Momentum (TANDEM) framework for wake modeling, in which the velocity deficit and wake-added turbulence evolve as dynamically coupled fields. The framework is based on a decomposition of the flow into near- and far-wake regions, reflecting the distinct physical character of the governing equations in each region. In the near wake, rotor-induced pressure gradients are significant, and the flow retains elliptic character. Downstream, pressure gradients associated with the rotor become weak and streamwise diffusion is small relative to advection, permitting the governing equations to be parabolized and marched downstream as an initial-value problem. Within each region, relevant ABL processes may differ and can be incorporated through first-principles modeling. The near- and far-wake descriptions are then coupled through quantities constrained by the governing conservation equations. Individual modeling choices—including the representation of rotor forcing, near-wake development, turbulence closure, and dissipation of TKE—can therefore be refined independently while retaining the same overall framework. Framed in this way, the TANDEM framework of co-evolving the far-wake velocity deficit and turbulence based on explicit, first-principles near-wake initial conditions is a scaffold upon which to build a new class of wake models. This modular structure provides a systematic alternative to models that describe the entire far-wake using a single empirical evolution law/shape or introduce separate empirical corrections for near-wake initial conditions or for individual ABL effects, such as wake-added mixing or wake skewing from wind veer.

We instantiate the TANDEM philosophy by extending the parabolic far-wake model of Klemmer and Howland (2025) into a fully closed, coupled set of prognostic equations for the streamwise momentum deficit and wake-added TKE, efficiently solved as an initial value problem. We extend a near-wake length model to incorporate the effects of wind veer on the onset of the turbulent far-wake, where the parabolic equations are valid. The wake initial condition is integrated with the Unified Momentum Model (Liew et al., 2024), which extends classical momentum theory to turbine yaw misalignment and high-thrust operation without empirical corrections. A one-equation turbulence closure scheme is adapted to generalize across stratified ABL and wake scales. We show that the proposed TANDEM model yields excellent predictions of velocity deficits and wake-added turbulence of single turbine wakes across a wide range of ABL stabilities. The model also yields lower error than existing wake models for a moderate-sized wind farm in standard, greedy control and when the farm uses wake steering. The TANDEM model accuracy, similar to other bottom-up wake models, degrades for very large wind farms, which motivates coupling to top-down entrainment models in future work.

The remainder of this study is organized as follows. Section 2 outlines the LES data used to calibrate the TANDEM model and evaluate the wake model predictions. In section 3, we derive a parabolized wake model which co-evolves the streamwise momentum deficit and the wake-added turbulence kinetic energy. Comparison wake models are given in section 4. Then, in section 5, we systematically benchmark the new TANDEM wake against LES data of single turbine wakes in stratified ABLs,

https://doi.org/10.5194/wes-2026-149
Preprint. Discussion started: 27 August 2026

wake superposition in small wind farms, and for wind farm flow control applications. We summarize our results in section 6 and offer avenues for future work and model improvements.

2 LES data

To assess the predictive capability of different wake models, we compare with concurrent-precursor ABL LES and controlled, synthetic turbulent inflow LES. In this section, we delineate between the LES data used in model calibration, given in section 2.1, and model testing and evaluation, given in section 2.2.

All LES cases are run with the open-source, incompressible flow solver PadéOps (Ghate and Lele, 2017; Howland et al., 2020). The filtered Navier–Stokes equations are solved on a regular grid with Fourier collocation in the horizontal (x and y) directions and a sixth-order compact finite difference in the wall-normal direction z (Nagarajan et al., 2003). A fringe region (Nordström et al., 1999) is used in the streamwise direction to restore the wake flow to freestream velocity when a turbine is present in the simulation. Time stepping is performed with a fourth-order Runge–Kutta method (Gottlieb et al., 2011) and subgrid stresses are closed with the sigma model (Nicoud et al., 2011). In all simulations, flow statistics are time-averaged after the flow has reached a statistically quasi-stationary state. Turbines are modeled with an actuator disk using a modified thrust coefficient $C_T' = 4/3$ unless otherwise specified, corresponding to $C_T = 0.75$ (Calaf et al., 2010), and the correction factor introduced by Shapiro et al. (2019) is used in all simulations. To simulate ABL inflow conditions, we perform LES using a concurrent-precursor method (Stevens et al., 2014). Furthermore, we use a synthetic turbulence inflow method introduced by Heck and Howland (2026) to perform simplified, controlled simulations of a turbine with independently varying TI and inflow veer. Additional numerical details for the LES solver and problem setups are included in appendix A.

2.1 Calibration data

To calibrate the TANDEM model, we perform LES of a single turbine in two different inflow cases. The first case is an actuator disk in uniform, turbulent inflow with $3, 5, 8\%$ inflow turbulence intensity (TI). We define TI $\equiv \sqrt{2k/3}/U_h$, where $k = \overline{u_i' u_i'}/2$ is the turbulence kinetic energy (TKE) and U_h is the wind speed magnitude at hub-height z_h. To complement the canonical case of uniform, turbulent inflow, we also perform two calibration LES cases of an actuator disk based on the IEA 15 MW reference wind turbine ($D = 240\,\mathrm{m}$, $z_h = 150\,\mathrm{m}$ Gaertner et al., 2020) in SBL inflow using the concurrent-precursor method (Stevens et al., 2014). Two simulations of the SBL are used for calibration varying $C_r = 0.3\,\mathrm{K\,h^{-1}}$ and $0.5\,\mathrm{K\,h^{-1}}$ (corresponding to $L_{\text{obu}} = 133\,\mathrm{m}, 75\,\mathrm{m}$, respectively). A surface roughness $z_0 = 1\,\mathrm{cm}$ is prescribed in both cases. These SBL simulations are only used to calibrate the wall mixing length in the TANDEM model. We emphasize that the wake model calibration only uses these specific single-turbine LES cases, whereas the testing data (described in section 2.2) will consist of out-of-sample configurations, including wind turbine arrays and unseen ABL stabilities.

https://doi.org/10.5194/wes-2026-149
Preprint. Discussion started: 27 August 2026

2.2 Testing data

To test the wake models in this study, we evaluate model predictions against unseen cases of single turbine wakes across a wide range of ABL stabilities and in synthetic turbulence inflows, four-row and ten-row yaw-aligned wind farms, and a wake steering case study using a 25-turbine wind farm. Compared with the calibration dataset, the testing dataset spans a wider range of stabilities ($L_{\text{obu}} \in [100\,\text{m}, 469\,\text{m}]$ and neutral stratification), controlled inflow simulations with up to $40°$ wind veer across the rotor (zero-veer, turublent inflow in the calibration data), and multi-turbine cases with up to 10 turbines in a row and a square wind farm with 25 turbines (only single-turbine cases in the calibration data). For single-turbine comparisons, both concurrent-precursor LES and synthetic turbulent inflow LES are used. We compare to wakes in veered inflow using the synthetic turbulent inflow method up to $40°$ veer across the rotor and for $\text{TI} \in 3, 5, 8\%$. Furthermore, we compare single-turbine wake model predictions against concurrent-precursor LES of an actuator disk in SBL inflow. The testing SBL data uses a $240\,\text{m}$-diameter actuator disk at $z_h = 150\,\text{m}$. The surface roughness is fixed at $z_0 = 10\,\text{cm}$ for the testing ABL simulations, and the cooling rate is varied between 0–$0.5\,\text{K}\,\text{h}^{-1}$.

For the wind farm comparisons, a four-turbine wind farm is simulated in a conventionally neutral boundary layer (CNBL) with inter-turbine spacing $S = 6D$ and varying inflow wind angles between $0°$ and $10°$, as measured by the angle between the freestream wind and the row of wind turbines. Positive angles denote an anti-clockwise rotation of the wind farm with the incident hub height flow, which is aligned with the x-direction. Additionally, a 25-turbine wind farm in CNBL inflow is used for a wake steering case study. For the wake steering study, a square 5×5 wind turbine array is rotated $42.5°$ anti-clockwise to create partial wake overlap that favors negative yaw misalignments. Finally, an aligned, ten-row wind farm is used to study the asymptotic behavior of various wake models in CNBL inflow conditions.

3 Model derivation

In this section, we derive the TANDEM wake model. We begin by defining the prognostic, parabolized equations for momentum and turbulence in section 3.1. Then, in section 3.2, we derive closure terms for the eddy viscosity and turbulence length scales of mixing and dissipation. Following this, we provide initial conditions and near-wake considerations, where elliptic properties of the pressure in the vicinity of the turbine are addressed, to complete the model in section 3.3.

3.1 Governing equations

We start with a double decomposition of the wake fields from the full flow, $u = \Delta u + u^B$, as well as a Reynolds decomposition to separate the mean flow $\bar{u}$ from the temporal fluctuations u'. Throughout this study, Δ is used to refer to the departure of the full flow from the base flow for a given flow quantity. The Reynolds decomposition is applied to both the full flow, $u = \bar{u} + u'$, as well as the wake flow, $\Delta u = \overline{\Delta u} + \Delta u'$. In the following sections, we will derive parabolic equations for the evolution of the mean wake momentum deficit $\overline{\Delta u}$ and the wake-added turbulence kinetic energy (TKE) $\Delta k \equiv k - k^B$, where $k \equiv \overline{u_i' u_i'}/2$ is the TKE in the full flow (and similarly for k^B).

https://doi.org/10.5194/wes-2026-149
Preprint. Discussion started: 27 August 2026

3.1.1 Deficit streamwise momentum

To arrive at a prognostic equation for the wake momentum, subtract the base RANS equations from the full RANS equations to yield (Martínez-Tossas et al., 2021):

$$\bar{u}_j \frac{\partial \overline{\Delta u}}{\partial x_j} = -\frac{\partial \overline{\Delta p}}{\partial x} - \frac{2}{Ro}\varepsilon_{1jk}\Omega_j \overline{\Delta u}_k - \overline{\Delta u}_j \frac{\partial \overline{u^B}}{\partial x_j} - \frac{\partial \Delta \overline{u' u'_j}}{\partial x_j} \tag{1}$$

where p is the non-dimensional pressure field and $\Delta \overline{u' u'_j} \equiv \overline{u' u'_j} - \overline{u^{B\prime} u^{B\prime}_j}$ is the wake-added Reynolds stress tensor. Similar to Martínez-Tossas et al. (2021) and Klemmer and Howland (2025), we assume that in the far-wake, the streamwise pressure gradient forcing is small compared with the Reynolds stress divergence. Note that streamwise pressure gradients are not negligible in the near-wake, which will be discussed in section 3.3. Furthermore, if the inflow is only a function of z and $\overline{\Delta w}$ is small, then the interaction term between the wake and base flow gradient is small, i.e., $\overline{\Delta w}\frac{\partial \overline{u^B}}{\partial z} \ll \overline{u}\frac{\partial \overline{\Delta u}}{\partial x}$ (Klemmer and Howland, 2024). In contrast to the lateral momentum budget, the Coriolis term is small in the streamwise momentum budget (Heck and Howland, 2025), and therefore we neglect it. Finally, we assume that the streamwise gradient of the Reynolds stress divergence is much smaller than the cross-stream gradients (c.f. Tennekes and Lumley, 1972).

The unclosed wake-added Reynolds stress tensor is modeled by introducing an eddy viscosity $\nu_T(x,y,z)$ used by Klemmer and Howland (2025) to yield

$$-\Delta \overline{u'_i u'_j} = 2\nu_T \Delta S_{ij}; \quad \Delta S_{ij} \equiv \frac{1}{2}\left(\frac{\partial \overline{\Delta u_i}}{\partial x_j} + \frac{\partial \overline{\Delta u_j}}{\partial x_i}\right). \tag{2}$$

After these simplifications, and substituting the eddy viscosity for the unclosed Reynolds stress divergence, we arrive at the model prognostic equation, which is parabolized as an initial value problem in the x-direction:

$$\frac{\partial \overline{\Delta u}}{\partial x} = \frac{1}{\bar{u}}\left[-\bar{u}_j \frac{\partial \overline{\Delta u}}{\partial x_j} + \frac{\partial}{\partial x_j}\left(\nu_T \frac{\partial \overline{\Delta u}}{\partial x_j}\right)\right], \quad j = 2,3. \tag{3}$$

The spatially-dependent eddy viscosity $\nu_T(x,y,z)$ is an unknown quantity which will be closed in section 3.2.

3.1.2 Wake-added turbulence

We begin with a prognostic equation for Δk, which is derived by subtracting the base-flow turbulence kinetic energy (TKE) equation from the full-flow TKE equation, as in Klemmer and Howland (2024). The result is

$$\bar{u}_j \frac{\partial \Delta k}{\partial x_j} = \Delta\mathcal{P} + \Delta\mathcal{B} + \Delta\mathcal{T} - \overline{\Delta u}_j \frac{\partial \Delta k}{\partial x_j} - \Delta\epsilon, \tag{4}$$

where $\Delta\mathcal{P}$, $\Delta\mathcal{B}$, $\Delta\mathcal{T}$, and $\Delta\epsilon$ are the shear production, buoyancy production/destruction, turbulent transport, and dissipation of wake-added TKE, respectively. As identified by Klemmer and Howland (2024), the contribution from the direct buoyancy term $\Delta\mathcal{B}$ is small, as is the advection by the wake flow $\overline{\Delta u}_j \frac{\partial \Delta k}{\partial x_j}$. These two terms are thus neglected, and the remainder of the terms in the TKE equation will be modeled.

We begin by modeling the shear production term, which is simplified under the following assumptions: (1) base Reynolds stresses are small compared to the wake-added terms; (2) gradients of the streamwise velocity drive turbulence production

https://doi.org/10.5194/wes-2026-149
Preprint. Discussion started: 27 August 2026

eawe european academy of wind energy
Open Access WIND ENERGY SCIENCE DISCUSSIONS

($i=1$ only); and (3) the dominant contributions to shear production are $j=2,3$. The resulting modeled wake-added shear production term, written in terms of the eddy viscosity, is

$$\Delta\mathcal{P} = -\Delta\overline{u_i'u_j'}\frac{\partial \bar{u}_i}{\partial x_j} - \overline{u_i^{B\prime}u_j^{B\prime}}\frac{\partial \overline{\Delta u_i}}{\partial x_j} \approx \nu_T \frac{\partial \overline{\Delta u}}{\partial x_j}\frac{\partial \bar{u}}{\partial x_j} \tag{5}$$

Likewise, the turbulence transport term is modeled using an eddy viscosity hypothesis:

$$\Delta\mathcal{T} \approx -\frac{\partial \overline{u_j'\Delta k}}{\partial x_j} \approx +\frac{\partial}{\partial x_j}\left(C_{k1}\nu_T\frac{\partial \Delta k}{\partial x_j}\right), \tag{6}$$

where $C_{k1}=1$ is a model constant (Klemmer and Howland, 2025). Finally, Taylor's dissipation surrogate is applied to model the dissipation of wake-added TKE such that

$$\Delta\epsilon \sim \frac{\Delta k^{3/2}}{\ell_\epsilon}, \tag{7}$$

where ℓ_ε is a length scale of dissipation.

In its final parabolized form, the prognostic equation for the wake-added turbulence Δk is:

$$\frac{\partial \Delta k}{\partial x} = \frac{1}{\bar{u}}\left[-\bar{u}_j\frac{\partial \Delta k}{\partial x_j} + \nu_T\frac{\partial \overline{\Delta u}}{\partial x_j}\frac{\partial \bar{u}}{\partial x_j} + \frac{\partial}{\partial x_j}\left(C_{k1}\nu_T\frac{\partial \Delta k}{\partial x_j}\right) - \frac{\Delta k^{3/2}}{\ell_\epsilon}\right]. \tag{8}$$

In eq. (8), summations are only over $j=2,3$ for both the transport and shear production terms, similar to eq. (3). To complete the model, the spatially heterogeneous eddy viscosity $\nu_T(x,y,z)$ and dissipation length scale ℓ_ϵ are closed in section 3.2.

3.2 Eddy viscosity turbulence closure

This work extends the one-equation $k-\ell$ closure for the eddy viscosity introduced by Klemmer and Howland (2025). In this formulation, the eddy viscosity $\nu_T = C_\nu \ell\sqrt{k}$, where ℓ is a master mixing length of the flow to be determined, and $k = k^B + \Delta k$ is the full TKE. Here, we will derive a mixing length formulation to close the wake model. Note that the streamwise evolution of Δk (eq. (8)) relies on $\bar{u} = u^B + \overline{\Delta u}$, so the wake-added turbulence depends on the wake deficit. Furthermore, from eq. (3), the evolution of the wake deficit Δu depends on the eddy viscosity, which is a function of Δk. Hence, there is an interplay between Δu and Δk which must be modeled in tandem – the co-evolution of the momentum and turbulence equations is critical to the generality and predictive success of the wake model.

We adopt a generalized mixing length approach to modeling ℓ, similar to Lopez-Gomez et al. (2020). The guiding philosophy used in this modeling approach is that a spatially dependent mixing length constrains the shear production of wake-added turbulence, which can be modulated by factors in the ABL such as surface layer scaling and buoyancy effects. The master length scale $\ell(x,y,z)$ is a function of the wake and background flow conditions and is used to compute the eddy viscosity ν_T. In section 3.2.1 and section 3.2.2, we derive two length scales, a dynamics-driven wake length scale ℓ_{md}, and a wall-limiting length scale ℓ_w derived from Monin–Obukhov similarity theory (MOST). We do not include a free-atmosphere mixing length in this work (c.f. Blackadar, 1962) because the wake length scale ℓ_{md} already limits the largest eddies in the flow. Therefore, the surface layer and wall proximity limitation is provided by MOST, and the wake and ABL-scale mixing length limitations

https://doi.org/10.5194/wes-2026-149
Preprint. Discussion started: 27 August 2026

are provided by $\ell_{\rm md}$. As such, the combination of these mixing lengths allows the mixing length model to be valid both within the surface layer and above it, where MOST is no longer valid. The master mixing length ℓ is the local minimum of these two length scales, such that $\ell(x,y,z) = \min(\ell_{\rm md}, \ell_w)$ (c.f. Lopez-Gomez et al., 2020). More mixing lengths or other blending functions could be added to account for additional effects in future work.

3.2.1 Minimum dissipation mixing length

The key mixing length scale is the minimum dissipation mixing length, $\ell_{\rm md}$, based on a regional balance of shear production of wake-added TKE (Δk) and dissipation of Δk (c.f., Abkar et al., 2016; Lopez-Gomez et al., 2020). The minimum dissipation length scale is derived by integrating the prognostic equation for Δk over the yz-domain. The resulting mixing length, $\ell_{\rm md}$, is a constrained minimization of the dissipation of wake-added turbulence such that production and dissipation are in balance.

We begin with the prognostic equation for Δk and assume that the local evolution of Δk in the streamwise direction is small compared with the production and dissipation terms. Assuming $\ell = \ell_{\rm md}$ (i.e., $\ell_{\rm md}$ is the smallest/limiting length scale in the flow), we substitute the $k-\ell$ mixing length closure into ν_T in the shear production term (eq. (5)). Then, integrating in the yz-plane (designated by the domain Ω) to remove the transport and advection terms yields

$$\iint_\Omega C_\nu \ell_{\rm md}\sqrt{k}\left(\frac{\partial \bar{u}}{\partial x_j}\frac{\partial \overline{\Delta u}}{\partial x_j}\right) dA = \iint_\Omega \frac{\Delta k^{3/2}}{\ell_\epsilon}\, dA. \tag{9}$$

To solve for a minimum dissipation mixing length, we assume that the dissipation length scale is proportional to the mixing length ℓ such that $\ell_\epsilon \sim \ell_{\rm md}$. Furthermore, we assume that the length scale of mixing $\ell_{\rm md}$ is approximately constant across the wake region and therefore can be factored out of both integrals. Rearranging yields an explicit expression for $\ell_{\rm md}$:

$$\ell_{\rm md} \equiv \left(\frac{\iint_\Omega \Delta k^{3/2}\, dA}{\iint_\Omega \sqrt{k}\left(\frac{\partial \bar{u}}{\partial x_j}\frac{\partial \overline{\Delta u}}{\partial x_j}\right) dA}\right)^{1/2}. \tag{10}$$

We drop the proportionality relation and the (yet to be determined) calibration coefficient C_ν in eq. (10) to yield our definition for the minimum dissipation mixing length $\ell_{\rm md}$. The minimum dissipation mixing length can be evaluated during model runtime because Δk, k, $\overline{\Delta u}$, and $\bar{u}$ are solved concurrently. Additionally, $\ell_{\rm md}$ does not rely on the geometry of the wake (such as a wake half-width), which can be ill-defined in the case of multiple wakes in superposition or in complex inflow conditions (e.g., veer). Next, we will calibrate C_ν using uniform, turbulent inflow LES data.

We can evaluate the model form by comparing $\ell_{\rm md}$ with the "true" mixing length $\ell \equiv \nu_T/\sqrt{k}$ using LES data. In fig. 1, we compute $\ell_{\rm LES} \equiv \nu_T/\sqrt{k}$ and $\ell_{\rm md}$ from LES data of an actuator disk-modeled turbine in uniform inflow conditions with an inflow turbulence intensity of $\mathrm{TI} = 5\%$ and $C_T' = 4/3$, corresponding to $C_T = 0.75$. The turbulent eddy viscosity $\nu_T(x,y,z)$ is computed with a pointwise least-squares regression between ΔS_{12} and $\Delta\overline{u'v'}$ and ΔS_{13} and $\Delta\overline{u'w'}$. The mixing length $\ell_{\rm LES}$ is computed pointwise and then averaged in y and z over the wake region (defined as the region where $\partial\bar{u}/\partial z > \max(\partial\bar{u}/\partial z)$ at a given x location). The downstream region beginning at the actuator disk and extending to $x/D = 15$ is shown.

As shown in fig. 1, there is near-linear proportionality between the true mixing length, ℓ, and the minimum dissipation mixing length, $\ell_{\rm md}$. Therefore, we conclude that $\ell_{\rm md}$ is a useful surrogate for the mixing length $\ell = C_\nu \ell_{\rm md}$ in the wind turbine

https://doi.org/10.5194/wes-2026-149
Preprint. Discussion started: 27 August 2026

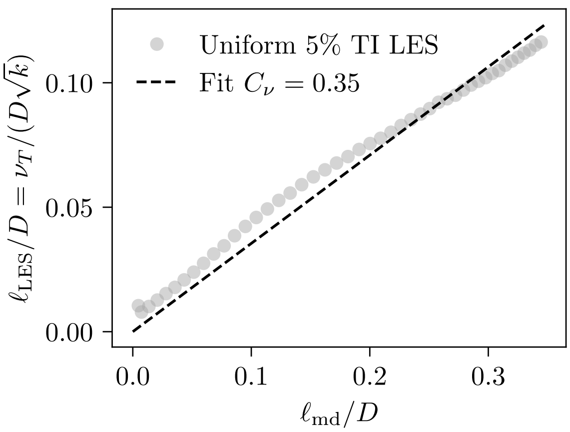

Figure 1. Turbulent mixing length $\ell_{\mathrm{LES}} \equiv \nu_T/\sqrt{k}$, fit from LES data of an actuator disk in $\mathrm{TI} = 5\%$ uniform, turbulent inflow, versus the minimum dissipation length scale ℓ_{md} derived in eq. (10). The slope of the relation yields the model coefficient C_ν, which is used throughout the study.

wake. The slope of proportionality between ℓ and ℓ_{md} is approximately $C_\nu = 0.35$, which is used throughout the remainder of this study.

When multiple wakes are present, the domain of integration Ω should not be the entire yz-plane. Rather, for eq. (10) to be valid, Ω must be sufficiently small such that ℓ_{md} is constant within the integration domain, but large enough that the transport terms integrate to zero. In *a priori* tests against LES data, we find that the mixing length is approximately constant within an individual wake, but may vary between wakes in a wind farm. Therefore, the boundaries of the integration domain Ω are chosen to be the midpoints between adjacent turbines. The resulting ℓ_{md} is linearly interpolated in the cross-stream direction (y) between turbines to yield a smooth, spatially dependent mixing length across the wind farm.

3.2.2 Atmospheric surface layer length scale

The ABL can also limit mixing due to the presence of the wall and/or stable stratification. Therefore, we also consider a surface layer (wall) mixing length ℓ_w in the minimization of the master mixing length ℓ. The surface layer mixing length in ABL conditions can be derived from Monin-Obukhov similarity theory. Near the wall, ℓ_w is small and therefore drives the eddy viscosity in the surface layer. As wall-normal distance increases, ℓ_w exceeds ℓ_{md}, so the dynamics-driven mixing length ℓ_{md} sets the eddy viscosity, and the surface layer scaling is not used. An additional free atmosphere/ABL height length scale is not used here because ℓ_{md} is assumed to limit the wake mixing length scale (i.e. $\ell_{\mathrm{md}} < \ell_{\mathrm{ABL}}$).

To derive an expression for ℓ_w, we begin with

$$\phi_m(\zeta) = \frac{\kappa z}{u_\star} \frac{\partial \bar{u}}{\partial z}, \tag{11}$$

https://doi.org/10.5194/wes-2026-149
Preprint. Discussion started: 27 August 2026

eawe european academy of wind energy
Open Access WIND ENERGY SCIENCE DISCUSSIONS

where $\zeta = z/L_{\text{obu}}$, L_{obu} is the Obukhov length, $u_\star$ is the friction velocity, and $\kappa = 0.4$ is the von Karman constant. Here, we define the empirical stability function for momentum $\phi_m(\zeta)$ as:

$$\phi_m(\zeta) = \begin{cases} 1+\beta_m\zeta, & \zeta \le 1, \\ 1+\beta_m, & \zeta > 1. \end{cases} \tag{12}$$

where $\beta_m = 5$ is recommended for $\kappa = 0.4$ (c.f. Brutsaert, 1982, pp. 65-72 and sources within).

Shear stress is assumed to be constant in the atmospheric surface layer, thus

$$\tau/\rho = u_\star^2 = \nu_T \frac{\partial \bar{u}}{\partial z}, \tag{13}$$

where ρ is the fluid density. We then write a Prandtl mixing length closure:

$$\nu_T \sim \ell_w^2 \left| \frac{\partial \overline{u^B}}{\partial z} \right|. \tag{14}$$

Because $\partial \overline{u^B}/\partial z > 0$ in the atmospheric surface layer, we drop the absolute value and substitute eq. (14) into eq. (13). Simplifying yields

$$\ell_w = C_w \frac{\kappa z}{\phi_m(\zeta)}, \tag{15}$$

where C_w is a constant of proportionality to be determined from LES data.

We tune the wall length scale parameter C_w using the calibration SBL LES dataset (see section A2 for numerical details and inflow parameters). In fig. 2, two cooling rates, $C_r = 0.3, 0.5\,\mathrm{K\,h^{-1}}$, are used and shown alongside the uniform, turbulent inflow data used to calibrate C_ν. The LES mixing length ℓ_{LES} is computed in the wake region from $x/D \in [0, 15]$ using the method described in section 3.2.1, and plotted against the minimum dissipation mixing length ℓ_{md}.

From fig. 2, it is clear that stability can affect the wake mixing length. At small ℓ_{LES}, the minimum dissipation scale ℓ_{md} is limiting and there is strong correlation between ℓ_{md} and ℓ_{LES}. However, as ℓ_{md} increases, the master (true) mixing length ℓ_{LES} in the SBL is limited by stability, and the maximum ℓ is a function of the cooling rate through the Obukhov length. We assume that this additional limiting length scale is thus a surface layer length scale and fit $C_w = 4$, where ℓ_w is computed from eq. (14) using $z = z_h = 150\,\mathrm{m}$. The constant $C_w = 4$ is used across all ABL stability regimes throughout this study.

3.2.3 Dissipation length scale

To close the Taylor dissipation surrogate, we determine an appropriate length scale of dissipation, ℓ_ε. Following dimensional analysis, the length scale of turbulence dissipation is given by the inverse of the slope of the line between the dissipation of wake-added turbulence, $\Delta\varepsilon$, and $\Delta k^{3/2}$. Using the uniform, $\mathrm{TI} = 5\%$ actuator disk LES data from section 3.2.1 to determine C_ν, we show a best-fit line between $\Delta\varepsilon$ and $\Delta k^{3/2}$, both non-dimensionalized, in fig. 3, for the region $x/D \in [0, 15]$. This calibration yields $\ell_\varepsilon \approx 0.78D$, which is used throughout this study for the TANDEM model.

https://doi.org/10.5194/wes-2026-149
Preprint. Discussion started: 27 August 2026

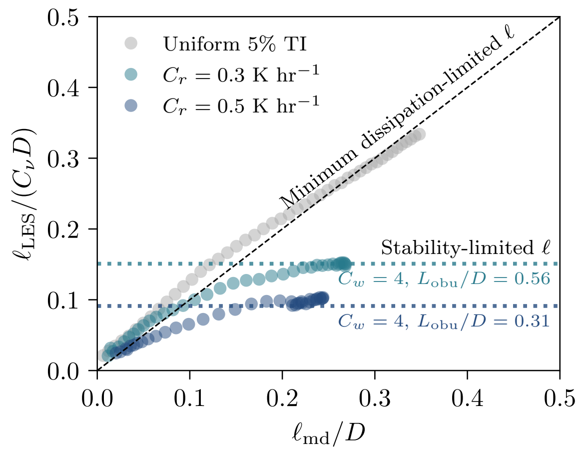

Figure 2. Mixing length computed using LES data in the SBL ($C_r = 0.3, 0.5\,\mathrm{K\,h^{-1}}$), normalized by $C_\nu = 0.35$, versus minimum-dissipation mixing length ℓ_{md}. The dashed black line shows 1:1 proportionality. The stability-limiting mixing length at hub height is assumed to be the maximum wake-averaged mixing length $\ell/(C_\nu D)$, which is used to calibrate $C_w = 4$. Uniform inflow data from fig. 1 is shown for reference.

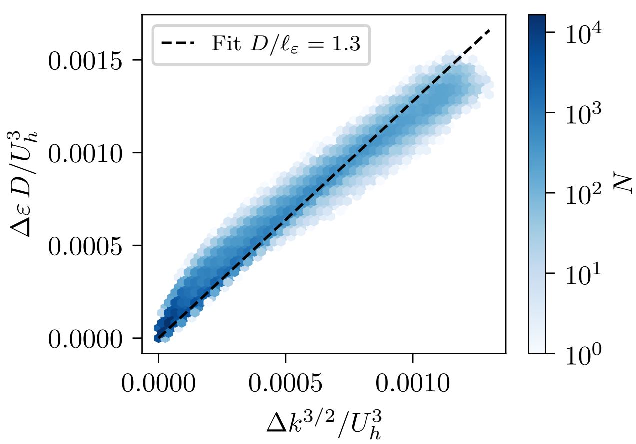

Figure 3. Log-scale hexplot of dissipation of wake-added TKE versus $\Delta k^{3/2}$. The best-fit slope yields the reciprocal of the dissipation length scale ℓ_ε, which is assumed to be constant.

3.3 Initial condition and near-wake model

290 As stated in section 1, a key decomposition we make in the TANDEM framework is to separate the near-wake and far-wake models. The parabolic far-wake equations for the wake-added TKE and deficit momentum are valid after pressure gradients and streamwise diffusion terms become negligible. We denote this location as the near-wake length $x = x_0$, which depends both on the inflow conditions and the turbine operating set point. The critical transition between the far-wake evolution and

https://doi.org/10.5194/wes-2026-149
Preprint. Discussion started: 27 August 2026

the aerodynamics at the rotor is dictated by the initial condition coupling between the near-wake ($x < x_0$) and the far-wake ($x \geq x_0$). Correct prediction of the far-wake requires both accurate near-wake modeling and physically consistent coupling between the flow zones.

The near-wake dynamics traditionally derive from classical momentum theory. Momentum theory relates the initial wake velocity defect δu_0 to the thrust coefficient of the rotor, $C_T \equiv 2|\boldsymbol{F}_T|/(\rho A_d U_h^2)$, through the induction factor $a_n = \frac{1}{2}(1 - \sqrt{1 - C_T})$. Here, ρ is the fluid density, $A_d = \pi D^2/4$ is the swept area of the rotor, $\boldsymbol{F}_T$ is the thrust force imparted by the turbine on the flow, and U_h is the hub height wind speed magnitude. Following momentum theory, $\delta u_0 = -2a_n U_h$. However, classical momentum theory does not generalize to cases of yaw misalignment or high rotor thrust coefficient without the use of empirical corrections that are typically fit to experimental data and therefore do not enforce physical constraints (Glauert, 1926; Madsen et al., 2020; Burton et al., 2011). Therefore, a novel extension of this work is to derive the wake initial condition from the Unified Momentum Model (UMM) (Liew et al., 2024), which is described in appendix B. The UMM accounts for the sidewash velocity induced by yaw misalignment with a lifting line model and circumvents empirical high-thrust corrections by using a fast, pretabulated pressure-Poisson solver in the near-wake. The resulting set of five coupled, nonlinear equations approximates the elliptical near-wake dynamics through mass, momentum, and energy conservation without relying on empirical corrections. The inputs to the UMM are the turbine operating set point C_T and γ (or equivalently the local thrust coefficient $C_T' = 2|\boldsymbol{F}_T|/(\rho A_d u_d^2)$, where u_d is the rotor-normal, rotor-averaged velocity). The outputs of the UMM are the streamwise and lateral wake velocities $u_4 = U_h + \delta u_0$ (which generalizes and replaces the δu_0 from momentum theory) and v_4, induction factor a_n, wake pressure Δp, and near-wake length x_0, which provide additional information about the near-wake beyond what is typically used in analytical wake models.

Momentum theory provides the mean velocity state after pressure recovery, but it does not provide the wake-added TKE required to initialize the coupled TANDEM equations at $x = x_0$. Existing models for near-wake turbulence are generally empirical (Crespo and Hernández, 1996; Ishihara and Qian, 2018; Khanjari et al., 2025) and would introduce a separately calibrated sub-model for $\Delta k(x_0)$. Moreover, velocity deficit and wake-added TKE develop together: rotor loading establishes the initial velocity shear, which generates turbulence as the near-wake shear layer grows and erodes the potential core. To avoid an empirical model for $\Delta k(x_0)$, we initialize the numerical solution at the rotor plane, $x = 0$, with the UMM-derived velocity deficit and zero wake-added TKE. We then march the coupled equations through a transition region, $0 < x < x_0$, using a distinct near-wake mixing length ℓ_{NW}. This modification initiates shear production, allows wake-added TKE to develop dynamically, and regularizes any sharp velocity gradients at the rotor. Thus, the near-wake marching zone is used as a coupling procedure between the UMM and the parabolic TANDEM equations to impose the initial momentum deficit condition and spin up wake-added TKE.

The remainder of this section describes each component of this coupling procedure. First, section 3.3.1 extends the near-wake length model to account for wake deformation by inflow wind veer. Next, section 3.3.2 constructs the velocity initial condition at the rotor plane from the UMM prediction. Finally, section 3.3.3 defines the modified mixing length used over $0 < x < x_0$ to generate wake-added turbulence and transition smoothly to the far-wake solution.

https://doi.org/10.5194/wes-2026-149
Preprint. Discussion started: 27 August 2026

3.3.1 Near-wake length closure in veered inflow

The near-wake length x_0, defined as the location where the wake velocity reaches its minimum value, dictates the onset of the turbulent far-wake where the TANDEM equations are valid. Previous work (Bastankhah and Porté-Agel, 2016; Liew et al., 2024) identified that x_0 depends on both inflow conditions, such as TI, and also turbine operation, such as C_T and γ. In Heck and Howland (2026), the near-wake length was noted to also depend on the inflow veer, but current models do not capture this behavior, limiting the efficacy of near-wake length models in veered inflow conditions such as the SBL (Klemmer and Howland, 2025). In this section, we derive a near-wake length model to account for the effects of incident wind veer, extending the work of Bastankhah and Porté-Agel (2016); Liew et al. (2024).

The near-wake ends and the far-wake begins when the shear layer has eroded the entire thickness of the wake. A primary effect of wind veer is to distort the near-wake region into an elliptical shape, which thins the wake core. Therefore, wind veer reduces the semi-minor axis $a_{\min}$ of the elliptical wake, which accelerates the rate at which the shear layer reaches the center of the wake. Yaw misalignment additionally modifies the initial wake cross-section. To capture the effects of wind veer and yaw-induced wake skewing on the near-wake length x_0, the variation of $a_{\min}$ with streamwise position x must be taken into account.

We begin by assuming that the veer is linear across the rotor such that $\psi(z) \approx -\alpha_{\rm v}(z - z_h)/D$, where $\alpha_{\rm v}$ is the inflow wind veer in radians across the rotor diameter. The skewed wake cross-section is then described by

$$\frac{(y-\delta(z))^2}{R_4^2 \cos^2\gamma} + \frac{(z-z_h)^2}{R_4^2} = 1, \tag{16}$$

where $\delta(z) = x\tan(\psi(z)) \approx -\alpha_{\rm v} x(z - z_h)/D$ is the lateral advection due to wind veer, z_h is the hub height, and γ is the yaw-misalignment angle. Following conservation of momentum, the initial wake width R_4 is given by (Liew et al., 2024):

$$\frac{R_4}{D} = \frac{1}{2}\sqrt{\frac{U_h(1-a_n)}{u_4}}. \tag{17}$$

where a_n and u_4 are output by the UMM.

We now solve for the semi-minor axis of the skewed ellipse, which is the thinnest region of the wake core. This is accomplished by transforming eq. (16) by a coordinate rotation to identify the principal axes. Applying the coordinate transformation $\tilde{z} = z - z_h$ and defining

$$q = \frac{\alpha_{\rm v} x}{D}, \tag{18}$$

the wake cross-section becomes

$$\frac{(y+q\tilde{z})^2}{\cos^2\gamma} + \tilde{z}^2 = R_4^2. \tag{19}$$

The sign of the cross-term depends on the sign convention used for $\alpha_{\rm v}$ and does not affect the principal-axis lengths. Expanding the quadratic terms gives

$$\frac{y^2}{\cos^2\gamma} + \frac{2q}{\cos^2\gamma} y\tilde{z} + \left(1 + \frac{q^2}{\cos^2\gamma}\right)\tilde{z}^2 = R_4^2. \tag{20}$$

https://doi.org/10.5194/wes-2026-149
Preprint. Discussion started: 27 August 2026

We can rewrite this in matrix form as

$$\begin{bmatrix} y & \tilde{z} \end{bmatrix} \begin{bmatrix} 1/\cos^2\gamma & q/\cos^2\gamma \\ q/\cos^2\gamma & 1+q^2/\cos^2\gamma \end{bmatrix} \begin{bmatrix} y \\ \tilde{z} \end{bmatrix} = R_4^2. \tag{21}$$

Applying a coordinate transformation that diagonalizes the 2×2 matrix aligns the coordinate axes with the principal axes of the ellipse. This is equivalent to the eigenvalue problem

$$\det\left(\begin{bmatrix} 1/\cos^2\gamma & q/\cos^2\gamma \\ q/\cos^2\gamma & 1+q^2/\cos^2\gamma \end{bmatrix} - \mathbf{I}\lambda \right) = 0, \tag{22}$$

where $\mathbf{I}$ is the 2×2 identity matrix. The corresponding characteristic polynomial is

$$\lambda^2 - \left[\frac{1+q^2}{\cos^2\gamma} + 1\right]\lambda + \frac{1}{\cos^2\gamma} = 0. \tag{23}$$

The eigenvalues determine the lengths of the principal axes. In particular, the semi-minor axis is $a_{\min} = R_4/\sqrt{\lambda_{\max}}$, where $\lambda_{\max}$ is the larger eigenvalue. Applying the quadratic formula gives

$$a_{\min} = R_4\sqrt{2}\left[\frac{1+(\alpha_{\mathrm{v}}x/D)^2}{\cos^2\gamma} + 1 + \sqrt{\left(\frac{1+(\alpha_{\mathrm{v}}x/D)^2}{\cos^2\gamma}+1\right)^2 - \frac{4}{\cos^2\gamma}}\right]^{-1/2}. \tag{24}$$

Now that we have an explicit function for the minimum shear-layer thickness required to completely erode the potential core, we solve for the shear-layer growth. We begin with the generalized model proposed by Lee and Chu (2003),

$$\frac{1}{u_\infty}\frac{\mathrm{d}s}{\mathrm{d}t} = \alpha \mathrm{TI} + \beta\frac{u_e}{u_\infty}. \tag{25}$$

Here, s is the shear-layer thickness and u_s is the characteristic shear-layer velocity, taken to be $(u_\infty + u_4)/2$, while $u_e = (u_\infty - u_4)/2$ is the characteristic velocity in the frame of reference of the shear layer (Bastankhah and Porté-Agel, 2016; Liew et al., 2024). The shear-layer growth parameter is $\beta = 0.14$ (Liew et al., 2024), and α is an empirical parameter for the influence of freestream turbulence intensity (TI) on shear-layer growth. Bastankhah and Porté-Agel (2016) reported $4\alpha = 2.32$ to fit their experimental wind-tunnel data for a scaled, three-bladed model turbine. However, we find that $\alpha = 2.0$ better matches the LES data of Heck and Howland (2026) for an actuator disk in uniform ($\alpha_{\mathrm{v}} = 0$), turbulent inflow conditions. Note that veered-inflow LES data are not used to calibrate α here; predictions of x_0 in veered inflow are out-of-sample and driven by the modeled skewing. After substituting u_s and u_e and separating variables, integration gives

$$s(x) = x\left(\beta\left|\frac{u_\infty - u_4}{u_\infty + u_4}\right| + \alpha I\left|\frac{2u_\infty}{u_\infty + u_4}\right|\right). \tag{26}$$

The end of the near-wake is demarcated by the location $x = x_0$ where $s(x_0) = a_{\min}(x_0)$. That is, the near-wake ends when the shear-layer thickness completely erodes the inviscid potential core. Therefore, equating $s(x_0)$ and $a_{\min}(x_0)$ and substituting

https://doi.org/10.5194/wes-2026-149
Preprint. Discussion started: 27 August 2026

for R_4 gives the following implicit equation, which can be solved efficiently by iteration:

$$\begin{aligned}&\frac{\sqrt{2}}{2}\sqrt{\frac{u_\infty(1-a_n)}{u_\infty+u_4}}\left[\frac{1+(\alpha_{\rm v}x_0/D)^2}{\cos^2\gamma}+1+\sqrt{\left(\frac{1+(\alpha_{\rm v}x_0/D)^2}{\cos^2\gamma}+1\right)^2-\frac{4}{\cos^2\gamma}}\right]^{-1/2}\\&\quad=\frac{x_0}{D}\left(\beta\left|\frac{u_\infty-u_4}{u_\infty+u_4}\right|+\alpha I\left|\frac{2u_\infty}{u_\infty+u_4}\right|\right).\end{aligned} \tag{27}$$

Equation (27) generalizes the near-wake length model of Bastankhah and Porté-Agel (2016); Liew et al. (2024) to additionally
385 account for inflow wind veer. For $\alpha_{\rm v}=0$ and $\mathrm{TI}=0$, eq. (27) reduces to the model of Liew et al. (2024). As a result of the skewing, increasing $|\alpha_{\rm v}|$ monotonically decreases the semi-minor axis and therefore also decreases x_0.

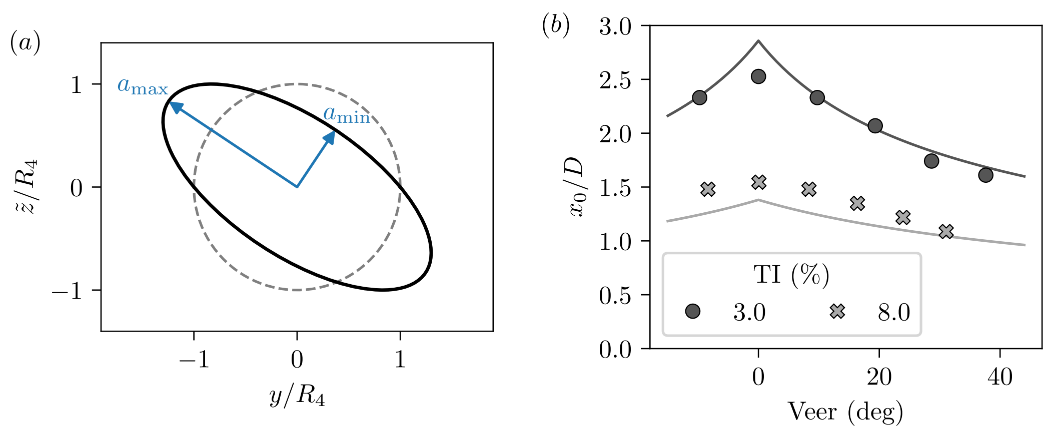

Figure 4. (a) Schematic of the veered near-wake. Skewing due to wind veer, approximated as a linear direction change with height, narrows the semi-minor axis $a_{\min}$ and elongates the semi-major axis $a_{\max}$. (b) Predictions of the near-wake model (eq. (27)) compared with the near-wake length as a function of inflow veer and turbulence intensity using LES data from Heck and Howland (2026).

3.3.2 Wake initial condition

The UMM is used to compute the initial wake velocity defect $\delta u_0 = u_4 - U_h$, where u_4 is output by the UMM equations. Next, the size of the initial wake velocity deficit must be determined. The initial wake profile and radius should conserve the
390 momentum defect integral at the near-wake location $x = x_0$ (Tennekes and Lumley, 1972; Ali et al., 2024),

$$M(x) \equiv \iint (U_h + \overline{\Delta u})\overline{\Delta u}\, dA\bigg|_x = -F_T\cos(\gamma)/\rho. \tag{28}$$

The momentum integral can be split into two components, a linear and quadratic term:

$$M(x) = U_h \iint \overline{\Delta u}\, dA\bigg|_x + \iint (\overline{\Delta u})^2\, dA\bigg|_x \tag{29}$$

https://doi.org/10.5194/wes-2026-149
Preprint. Discussion started: 27 August 2026

For a diffusion process, the linear term is conserved, while the quadratic term will strictly decrease (Ali et al., 2024). As $\Delta u < 0$, the decreasing quadratic term through wake diffusion will cause the combined momentum integral to become increasingly negative, resulting in an excess of deficit momentum downstream. That is, enforcing $M(0) = -F_T \cos\gamma/\rho$ results in $M(x_0) < -F_T \cos\gamma/\rho$, such that the integral momentum is correct at the rotor location but not necessarily conserved by the time it reaches x_0. Therefore, the goal of this section is to select an initial wake radius R_d such that the momentum deficit integral is matched at the onset of the far-wake, $M(x_0) = -F_T \cos\gamma/\rho$.

By approximating the near-wake as a diffusion process of a potential core where the maximum velocity defect magnitude is constant for $x < x_0$, an analytical formulation for R_d can be obtained; a full derivation, following Ali et al. (2024), and additional assumptions are provided in appendix C. Here, we provide the initial wake width R_d for an initial wake velocity distribution of depth δu_0 with Gaussian smoothing σ_{IC} for numerical stability, sketched in fig. 5(a). The result is an implicit expression (eq. (C6) in appendix C) for $R_d^{\mathrm{corr}}(C_T'; \sigma_{\mathrm{IC}})$ which can be efficiently solved using fixed-point iteration or pre-tabulated. The resulting initial radius is shown in fig. 5(b, c).

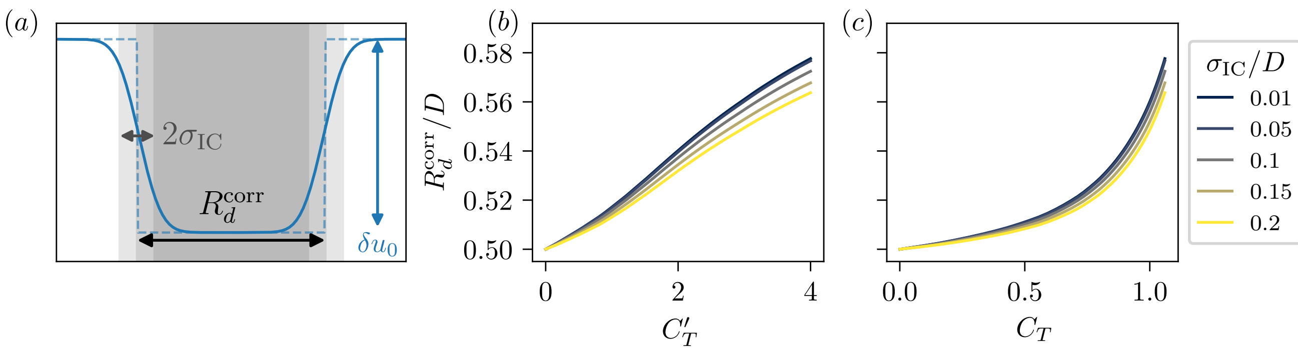

Figure 5. (a) Schematic of the Gaussian-smoothed top hat initial condition. (b) Momentum-corrected initial deficit radius R_d^{corr} as a function of local thrust coefficient C_T'. (c) Same as (b) but plotted against C_T.

3.3.3 Near-wake dynamics

The goal of the near-wake region is to transition between the near-wake and far-wake models and provide a physically consistent initial condition at the matching location $x = x_0$. As such, the turbulent mixing in the near-wake ($x < x_0$) should be strong enough to generate wake-added turbulence and erode the shear layer in the wake core, but not strong enough to start wake recovery (i.e., the centerline wake velocity deficit does not begin to decrease until $x > x_0$). To satisfy these conditions, we prescribe a near-wake mixing length ℓ_{NW} to linearly increase from zero to σ_{IC} (the shear layer width of the smoothed wake initial condition, see section 3.3.2) between the turbine location and $x = x_0$. If the new turbine is located in the wake of another turbine such that the mixing length at the new turbine location $\ell > 0$, then the background mixing length for that turbine is cached and stored as ℓ_0, from which the near-wake length continues to linearly increase. In summary, the eddy vis-

https://doi.org/10.5194/wes-2026-149
Preprint. Discussion started: 27 August 2026

eawe european academy of wind energy
Open Access WIND ENERGY SCIENCE DISCUSSIONS

cosity $\nu_T = C_\nu \ell \sqrt{k}$ depends on a mixing length, which has a prescribed linear spreading in the near-wake and switches to the generalized minimum mixing length in the far-wake:

$$\ell = \begin{cases} \min(\ell_{\mathrm{md}}, \ell_w, \ldots), & x \geq x_0; \\ \sigma_{\mathrm{IC}} x / x_0 + \ell_0, & x < x_0. \end{cases} \tag{30}$$

3.4 TANDEM wake model summary

For completeness, we will give a summary of the TANDEM wake model here, with key equations reproduced in this section. The TANDEM wake model solves two parabolic PDEs in a coupled forward-marching framework, one for the deficit momentum $\overline{\Delta u}$ (eq. (3)), and one for the wake-added TKE Δk (eq. (8)). The unknown eddy viscosity is closed with a generalized, spatially-dependent mixing length model that is the minimum of two candidate mixing lengths: (1) a minimum-dissipation mixing length ℓ_{md} and (2) a Monin–Obukhov mixing length ℓ_w. The near-wake of the rotor is solved with momentum theory, and here we use the Unified Momentum Model to generalize across yaw misalignment and high-thrust operation (Liew et al., 2024). The separation between the near-wake and far-wake is critical because the TANDEM model equations are only valid in the far-wake where streamwise pressure gradients are negligible. The initial condition is therefore selected such that upon diffusing to the onset of the far-wake, delineated by the point $x = x_0$, the wake conserves the momentum defect integral equal to the thrust imparted by the rotor. We derive a generalized model for the near-wake length (x_0, given by eq. (27)) that depends on the turbine thrust coefficient, inflow turbulence intensity, and inflow wind veer. A near-wake mixing length ℓ_{NW} is prescribed to spin up turbulence in the near-wake ($x < x_0$), given by eq. (30). The chosen model parameters and calibration source are summarized in section 3.4. An open-source, Python implementation of the TANDEM wake model is available in MITWindfarm [1].

Table 1. Summary of TANDEM wake model parameters and calibration source.

	Parameter	Value	Calibration source
Far-wake model constants	C_ν	0.35	Uniform, 5% TI LES case
	C_{k1}	1	Taken from Klemmer and Howland (2025)
	C_w	4	SBL LES cases, $L_{\mathrm{obu}} = 75\,\mathrm{m}, 133\,\mathrm{m}$
	ℓ_ε / D	0.78	Uniform, 5% TI LES case
Near-wake model constants	α	2.0	Uniform, $\mathrm{TI} \in 3\%; 8\%$ LES
	β	0.1403	Taken from Liew et al. (2024)
Numerical parameters	Δ_x	Variable	Dynamic (`scipy` RK-23 IVP solver, Bogacki and Shampine, 1989)
	Δ_y, Δ_z	$0.1D$	Model grid convergence tests
	σ_{IC}	$\sqrt{\Delta_y \Delta_z}/2$	Uniform, 5% TI LES case
	ℓ_{NW}	σ_{IC}	Uniform, 5% TI LES case

[1] https://github.com/Howland-Lab/MITWindfarm/

https://doi.org/10.5194/wes-2026-149
Preprint. Discussion started: 27 August 2026

4 Comparison wake models

In this study, we will investigate the ability of various fast-running engineering wake models to predict the velocity deficit behind an actuator disk model in sheared and veered ABL conditions. This section describes each wake model that will be tested, alongside the input parameters as well as any free parameters that are chosen for model calibration. All models predict the time-mean wake velocity deficit field $\overline{\Delta u} = \overline{u} - \overline{u^B}$.

4.1 Eddy viscosity closures for parabolized wake models

In section 3, we re-derived a prognostic equation for the evolution of wake momentum ($\overline{\Delta u}$) presented initially by Martínez-Tossas et al. (2021). The parabolic governing equation requires an eddy viscosity turbulence closure and initial and boundary conditions. In section 3.2, we introduce a new turbulence closure based on a generalized mixing length model. However, other closures for $\nu_T(x,y,z)$ have also been proposed. In subsequent subsections, we will briefly describe two alternative eddy viscosity closures.

4.1.1 Curled wake model

Martínez-Tossas et al. (2019, 2021) originally closed the eddy viscosity with a generalized mixing length formulation that interpolated between a surface layer mixing length κz and a free atmosphere mixing length (Blackadar, 1962). Imposing a Prandtl mixing length closure, the eddy viscosity is defined as $\nu_T = C\ell^2 \left|\frac{\partial U}{\partial z}\right|$, where $U(z) = [u^B(z) + v^B(z)]^{1/2}$ is the background velocity magnitude. Martínez-Tossas et al. (2021) recommended the empirical constant $C = 4$ by calibrating their model to SCADA data to account for additional mixing due to wakes that is not present in the background ABL flow, which we use in this study.

4.1.2 Scott model

Using scaled wind tunnel experiments and LES, Scott et al. (2023) proposed that the eddy viscosity evolves following a Rayleigh distribution. By assuming that the eddy viscosity scales with the wake velocity $u_4 = U_h\sqrt{1-C_T}$ multiplied by a length scale (chosen to be the rotor radius $R = D/2$), they defined eddy viscosity as

$$\nu_T = \frac{1}{2} R U_h \sqrt{1-C_T}\left[0.01 + \frac{x}{\sigma^2}\exp(-x^2/\sigma^2)\right]. \tag{31}$$

The width parameter $\sigma = 5.5$ was fit to LES data by Scott et al. (2023), along with the constant empirical offset of 0.01.

4.1.3 $k-\ell$ model

The current study extends the work of Klemmer and Howland (2025), where a one-equation $k-\ell$ eddy viscosity closure was proposed in the form of $\nu_T = C_{\nu'}\ell\sqrt{k}$. In the original $k-\ell$ study, Klemmer and Howland (2025) assumes that the mixing length ℓ scales with the hub-height wake width, measured where $\overline{\Delta u}$ recovers to 5% of U_h, and $C_{\nu'} = 0.04$ was calibrated to LES data. Then, a prognostic equation for the wake-added turbulence (eq. (8)) is marched concurrently with the streamwise

https://doi.org/10.5194/wes-2026-149
Preprint. Discussion started: 27 August 2026

eawe european academy of wind energy
Open Access WIND ENERGY SCIENCE DISCUSSIONS

momentum deficit equation. The dissipation length scale is assumed equal to the mixing length, $\ell_\varepsilon = \ell$. To limit mixing in the near-wake ($x < x_0$), the mixing length is assumed to be the wake diameter D, and only the inflow turbulence $\sqrt{k^B}$ is used in the eddy viscosity. No x_0 formulation was given in Klemmer and Howland (2025); instead, x_0 values were provided *a priori* from LES data. In this study, we use the near-wake length model for x_0 from section 3.3.1 so that the model is fully predictive and does not require information from LES beyond the inflow profiles and turbine thrust coefficient.

4.2 Analytical models

Most engineering wake models are fast-running, analytical expressions. A popular form of analytical wake modeling is Gaussian-based wake models (Bastankhah and Porté-Agel, 2014), where the far-wake assumes a self-similar Gaussian shape. In this section, we describe two popular Gaussian-based wake models. Then, we briefly describe the assembly of multiple analytical wake models in a wind plant solver by using a wake superposition model and a simple wake-added turbulence intensity model.

4.2.1 Gaussian wake model

The Gaussian wake model (Bastankhah and Porté-Agel, 2014, 2016) (abbreviated "Gaussian" throughout this study) assumes a self-similar, two-dimensional Gaussian velocity deficit profile $\overline{\Delta u}$ in the far-wake of a wind turbine. The Gaussian model is exactly the same as the model description from Bastankhah and Porté-Agel (2016), except that a turbulence intensity-dependent, linear wake-spreading rate $k_w = 0.3837 \cdot \mathrm{TI} + 0.004$ is adopted, following Niayifar and Porté-Agel (2016). In the Gaussian model, the near-wake length model for x_0 given by Bastankhah and Porté-Agel (2016) is in the Gaussian model rather than the near-wake length model derived in section 3.3.1.

4.2.2 Skewed vortex sheet model

The vortex sheet model, derived by Bastankhah et al. (2022), builds upon the Gaussian wake model to approximate the curled wake shape in yaw-misaligned rotor operation (Howland et al., 2016). By describing the wake shape as the evolution of a vortex sheet, which deflects and distorts due to its self-induced velocity, the vortex sheet model captures some non-axisymmetric effects of the structure of curled wakes trailing yaw-misaligned wind turbines. In veered inflow conditions, the wind direction changes as a function of height in the ABL, with rightward turning winds as a function of increasing height in the northern hemisphere following the Ekman spiral. The lateral flow introduced by wind veer distorts the wind turbine wake (Abkar and Porté-Agel, 2016). Building on the vortex sheet model, Mohammadi et al. (2022) and Narasimhan et al. (2025) included the veer advection term $y_{c,\text{veer}} = x\tan(\psi)$ from Abkar et al. (2018) to skew the wake from the incident wind veer, and requires $\psi(z)$ as an additional input variable. In this way, the skewed vortex sheet model (abbreviated "Vortex" throughout this study) is a direct extension and generalization of the skewed wake model of Abkar et al. (2018) to yaw-misaligned rotor operation.

The Vortex model used in this study is exactly the same as the model described in Narasimhan et al. (2022), which generalizes both Bastankhah et al. (2022) and Abkar et al. (2018). The inputs to the wake model are the turbine thrust coefficient C_T, yaw angle γ, inflow profile $\boldsymbol{u}^B(z)$, and hub-height turbulence intensity TI. When the turbine is yaw misaligned, the non-dimensional friction velocity $u_\star/U_h$ is also an input to model the decay of counter-rotating vortices in the ABL (Shapiro et al., 2020). The wall reflection is included by providing the turbine hub height z_h. We note that we do not use the ABL parameterization given by Narasimhan et al. (2025), instead using the exact LES inflow as the model input.

4.2.3 Superposition and wake-added turbulence models

When considering an array of turbines, the analytical wake models in sections 4.2.1 to 4.2.2 need to be superimposed together. Here, we use the modified linear superposition method introduced by Niayifar and Porté-Agel (2016). Furthermore, the wakes of downstream wind turbines are observed to mix more rapidly than the wakes of freestream turbines due to enhanced mixing from wake-added turbulence. For the analytical models, we use the empirical Crespo and Hernández (1996) model for wake-added turbulence intensity, $\mathrm{TI}_+ = 0.73 a_n^{0.8325} \mathrm{TI}_0^{-0.0325} (x/D)^{-0.32}$, where TI_0 is the turbulence intensity at the rotor plane, which includes upstream turbine wakes. Wake-added turbulence is added to the ambient turbulence intensity by summing squares, i.e., $\mathrm{TI}^2 = (\mathrm{TI}^B)^2 + \mathrm{TI}_+^2$, where TI^B is the turbulence intensity of the base flow. Following the guidelines of Niayifar and Porté-Agel (2016), the empirical wake-added turbulence intensity is distributed along a Gaussian distribution with a wake width twice the velocity deficit width.

5 Results

The results are organized as follows. First, in section 5.1, we evaluate the engineering wake models against LES velocity and turbulence fields of lone wind turbine wakes across a variety of inflow conditions. Then, in section 5.2, we compare wake model predictions to LES for a small 4-turbine wind farm in a conventionally neutral ABL. In section 5.3, we investigate the wake model predictions in a wind farm control case study using a 25-turbine wind farm in a conventionally neutral ABL. Finally, we conclude in section 5.4 with a 10-row wind farm, highlighting challenges and opportunities for future work in wind farm flow engineering modeling.

5.1 Single turbine wake model testing

In this section, we begin by evaluating the wake models in simplified inflow conditions where wind veer is controlled in isolation of wind shear, turbulence intensity, and other variables in section 5.1.1. Then, in section 5.1.2, we test the wake model velocity and turbulence predictions across ABL stratification regimes.

5.1.1 Wake recovery and structure in controlled veered conditions

Wind veer in the ABL affects several aspects of wake evolution, including wake skewing due to lateral flow (Abkar and Porté-Agel, 2016; Churchfield and Sirnivas, 2018) and enhanced wake recovery (Churchfield and Sirnivas, 2018; Heck and Howland, 2026). Existing wake models struggle to capture both of these effects, which we will investigate in this section, beginning with the skewed wake structure. Skewing impacts downstream turbines because the lateral flow advects the wake away from turbines

https://doi.org/10.5194/wes-2026-149
Preprint. Discussion started: 27 August 2026

eawe european academy of wind energy
Open Access WIND ENERGY SCIENCE DISCUSSIONS

directly downstream. Some engineering models, such as the Vortex model (Narasimhan et al., 2022; Mohammadi et al., 2022), incorporate a skewed wake correction term that passively advects the wake shape laterally with the inflow wind direction $\psi(z)$ (Abkar et al., 2018). However, the authors of these models have noted that passively advecting the wake with the lateral inflow overestimates the amount of skewing (Narasimhan et al., 2025). The parabolized RANS engineering models explicitly model the lateral advection due to wind veer. This work hypothesizes that by resolving key wake physics, such as the elongation of velocity gradients due to wind veer, parabolized RANS models will better capture the non-axisymmetric wake shape in veered inflow conditions.

Here, we compare the wake model predictions against LES of an actuator disk in veered inflow performed with a synthetic inflow LES method (Heck and Howland, 2026). To compare the wake shapes, we use the simulations from Heck et al. (2026) with veered, $\mathrm{TI} = 5\%$ inflow. The prescribed wind veer is approximately $\alpha_\mathrm{v} = 15^\circ$ turning across the rotor extent. The wind shear is zero in all simulations ($\partial U/\partial z = 0$) and the actuator disk is centered vertically to avoid interactions with the wall. In fig. 6, we show contours of the time-averaged wake velocity deficit at various downstream positions. Contour lines are drawn where the wake velocity is one e-folding less than the maximum wake velocity magnitude for each downstream location (i.e., $\overline{\Delta u} = 0.37\min(\overline{\Delta u}(y,z))$). Wake model predictions are compared to the LES contours (in black) in each panel.

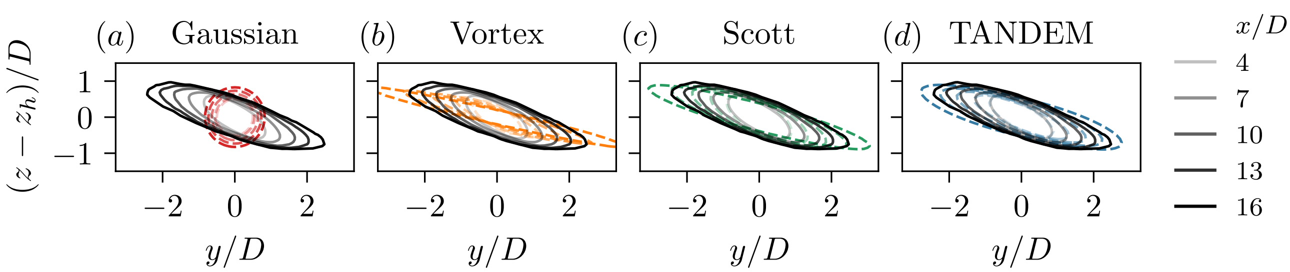

Figure 6. Contours of wakes in veered inflow conditions with 15° of total turning across the rotor extent at various downstream distances. Lines denote where the wake reaches 37% of the maximum magnitude at each downstream location. Wake model predictions are overlaid: (a) Gaussian model, (b) Vortex model, (c) Scott model, (d) TANDEM model. LES data from Heck et al. (2026).

In the absence of wall effects, wakes skew into an ellipse-like shape. The Gaussian model, which does not have a wind veer correction term, does not capture the wake skewing (fig. 6(a)). The Vortex model, shown in fig. 6(b), overpredicts the magnitude of wake skewing, and wakes become increasingly elongated and vertically shortened with increasing downstream distance. By contrast, the parabolized models show a significant improvement over the analytical models in capturing the skewed wake shape. Specifically, the TANDEM model displays excellent agreement with the LES wake shape, only slightly overpredicting the skewness. We hypothesize that the coupling between the wake-added turbulence and wake velocity deficit, which is not present in the Scott model, contributes to the progressive improvement in skewed wake shape.

In addition to the lateral advection of the wake, wind veer has been observed to enhance the rate of wake recovery (Abkar and Porté-Agel, 2016; Churchfield and Sirnivas, 2018). Using the synthetic inflow method, Heck and Howland (2026) showed

https://doi.org/10.5194/wes-2026-149
Preprint. Discussion started: 27 August 2026

that the enhanced wake recovery in veered conditions can be attributed to increased turbulence entrainment from aloft, due to the elongation of the wake. However, analytical models, such as the Gaussian and Vortex models, do not include a mechanism for the increased wake recovery (i.e., increased wake spreading) as a function of wind veer. In fig. 7, the centerline wake velocity deficit (i.e., $\overline{\Delta u}_c = \overline{\Delta u}(x, 0, z_h)$) is shown as a function of wind veer and inflow TI using a synthetic turbulent inflow method at a hub height of $z_h/D = 0.625$ (Heck and Howland, 2026). The analytical Gaussian and Vortex model predictions are overlaid in orange and red, respectively, and the TANDEM model predictions are shown with the circle markers.

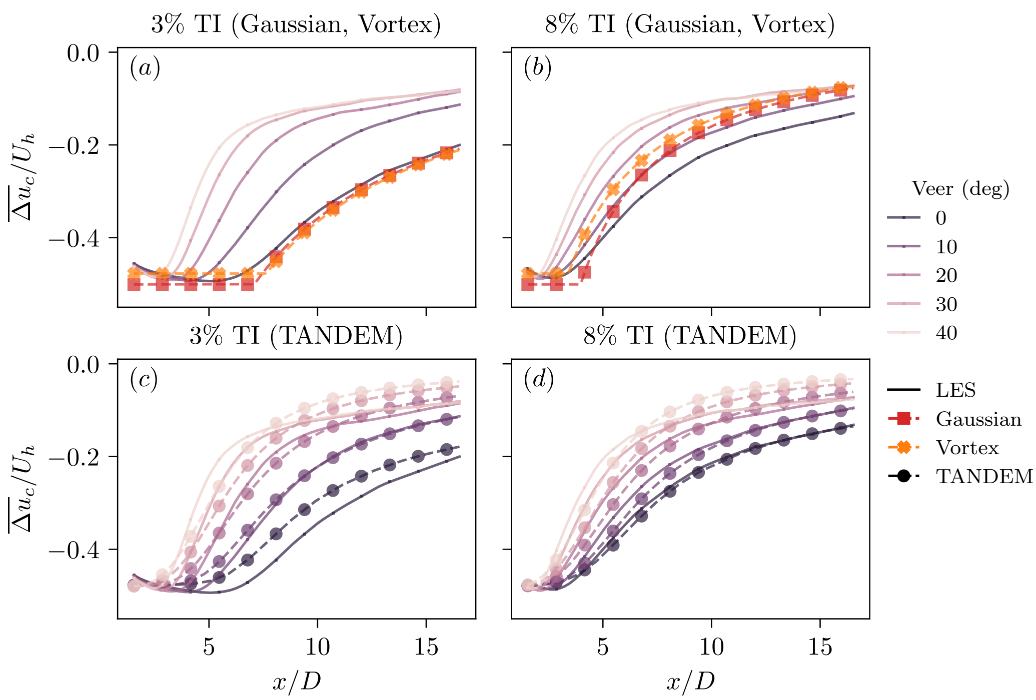

Figure 7. Centerline wake velocity deficit $\overline{\Delta u}_c$ as a function of downstream distance and inflow magnitude, for (*a*, *c*) TI = 3%, (*b*, *d*) TI = 8%. LES data are shown in solid lines (all subplots). (*a*, *b*) Gaussian and Vortex model predictions, which depend only on TI (but not veer). (*c*, *d*) TANDEM model predictions.

While the Gaussian and Vortex model predictions, shown in fig. 7(*a*, *b*), lie close to the $\alpha_\text{v} = 0°$ line, which depends on TI, there is no dependence of the wake recovery rate on the wind veer magnitude. Note that only one line is present for each model because the centerline deficit has no dependence on veer: different veer magnitudes return the same centerline deficit prediction. In theory, one could calibrate k_w(veer) to match these LES data, but increasing k_w would exacerbate the over-skewing in fig. 6 and may not generalize across ABL conditions. By contrast, the TANDEM model (fig. 7(*c*, *d*)) encodes the enhanced wake recovery with increasing wind veer magnitude through the resolved flow physics, without any veer-specific calibration. That is, the model parameters C_ν and l_ε that are calibrated to one LES case in uniform, turbulent inflow generalize well across TI and

https://doi.org/10.5194/wes-2026-149
Preprint. Discussion started: 27 August 2026

veer conditions. By resolving the flow physics interactions between the wake velocity deficit and the wake-added turbulence, the TANDEM model is able to generalize to out-of-sample flow conditions.

5.1.2 Wakes in stratified ABLs

In the stably stratified atmospheric boundary layer (SBL), thermal gradients affect the flow dynamics, suppressing turbulent motions and creating phenomena such as low-level jets and strong wind veer (Mahrt, 2014). As a result, engineering wake models often neglect key processes in the SBL, leading to deteriorated predictive accuracy (Klemmer and Howland, 2025). In this section, we evaluate the wake models described in sections 3 and 4 in neutrally and stably stratified inflow conditions, using concurrent-precursor LES of the stratified ABL as a reference (see section A2). Six simulations varying the surface cooling rate between $C_r = 0.0\,\mathrm{K\,h^{-1}}$ and $0.5\,\mathrm{K\,h^{-1}}$ are simulated with $z_0 = 10\,\mathrm{cm}$ in all cases, and a $240\,\mathrm{m}$-diameter actuator disk ($C'_T = 4/3$) is placed at $z_h = 150\,\mathrm{m}$ to generate a wake. The $C_r = 0$ case represents a truly neutral boundary layer (TNBL), also known as the turbulent Ekman layer. A summary of the inflow conditions is given in table 2. The power law exponent, used here as a diagnostic parameter, is computed using a reference height of z_h. Integral length scales of turbulence L_0^x and L_0^y are computed using autocorrelations of the hub-height streamwise velocity fluctuations taken in the x and y directions, respectively.

Table 2. Summary of ABL LES inflows. All simulations share a surface roughness of $z_0 = 10\,\mathrm{cm}$, geostrophic wind speed of $G = 12\,\mathrm{m\,s^{-1}}$, and latitude of $\phi = 45°$.

C_r ($\mathrm{K\,h^{-1}}$)	U_h ($\mathrm{m\,s^{-1}}$)	Power law exp.	Veer α_v (deg)	ψ_h (deg)	$u_\star$ ($\mathrm{m\,s^{-1}}$)	L_obu (m)	TI (%)	L_0^x (m)	L_0^y (m)
0	9.6	0.17	3.1	0.1	0.53	∞	8.2	312	82
0.1	9.4	0.3	13.1	0.2	0.44	469	5.2	63	21
0.2	9.7	0.34	17.6	0.3	0.41	249	4.5	46	18
0.3	10	0.38	22.9	0.2	0.4	170	4	43	16
0.4	10.4	0.41	29.1	-0.1	0.38	128	3.6	39	15
0.5	10.8	0.44	35.3	-0.6	0.36	100	2.9	38	14

In fig. 8, we show the centerline wake velocity deficit as a function of downstream distance and cooling rate. Contrary to common intuition (c.f. Xie and Archer, 2017), wakes recover more rapidly with increasing cooling rate (increasing stratification) in the SBLs simulated here, despite the decreasing inflow TI with increasing cooling rate. Analytical model predictions, which only parameterize wake spreading based on the incident TI (or friction velocity $u_\star$ (c.f. Narasimhan et al., 2025), which has a similar trend to TI) on wake recovery, predict the wrong trend: as stability increases, TI decreases, so the model predicts a slower wake recovery, as shown in fig. 8(a). Thus, analytical models lack critical physical processes underlying wake recovery in SBLs, leading to divergent predictions relative to LES. Note that the Gaussian model is shown, but the centerline wake recovery between the Gaussian and Vortex models is very similar (see fig. 7), as both models depend on the same parameterization of $k_w(\mathrm{TI})$ (Niayifar and Porté-Agel, 2016).

https://doi.org/10.5194/wes-2026-149
Preprint. Discussion started: 27 August 2026

WIND ENERGY SCIENCE DISCUSSIONS

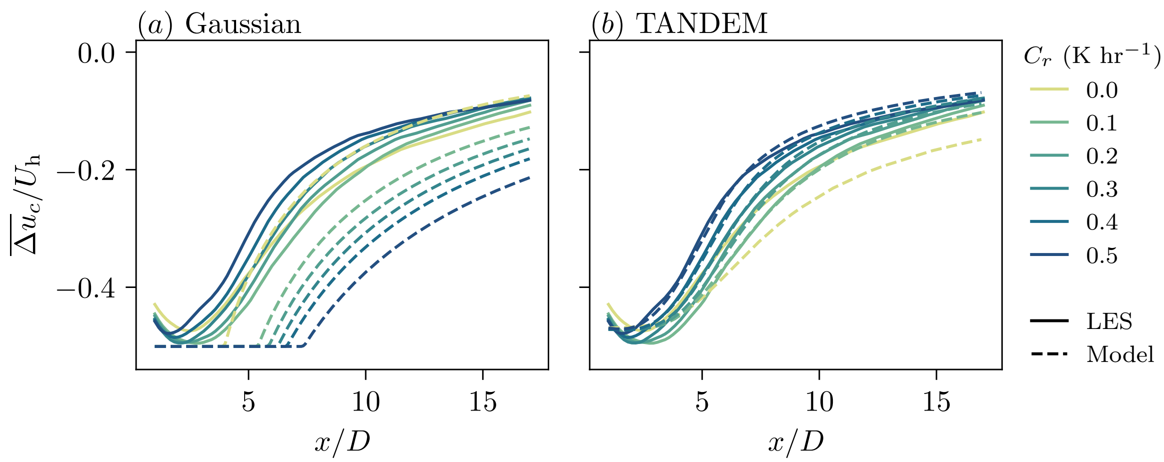

Figure 8. Centerline wake velocity deficit, as a function of downstream distance, for varying cooling rates in the stably stratified ABL. SBL LES reference data are shown in solid lines, while dashed lines show model predictions using the (a) Gaussian model and (b) TANDEM model.

As was noted by Heck and Howland (2026), at low TI, wind veer significantly modulates the wake dynamics and leads to enhanced wake recovery. The TANDEM model resolves the enhanced turbulent entrainment of momentum (due to stretched gradients of $\overline{\Delta u}$) that increases mixing with increased veer magnitude. This enhanced mixing offsets the reduced TI to increase
585 wake recovery with increasing cooling rate. As a result, the TANDEM model produces an excellent prediction of the wake recovery, particularly in the SBL. A slight underprediction in recovery in the recovery in TNBL inflow conditions is observed. We believe this divergence is due to additional lateral mixing from wake meandering induced by the large integral length scales of turbulence in the TNBL. As the freestream turbulence length scale can influence wake dynamics and recovery (c.f., Ghate et al., 2018; Hodgson et al., 2023; Vahidi and Porté-Agel, 2024; Bourhis et al., 2025), future work should address incorporating
590 the ABL turbulence length scale, which differs from surface layer theory, to improve the generalized mixing length formulation in deep boundary layers or convective conditions.

The TANDEM model receives nearly the same input data as the Vortex model (wind profiles, turbine geometry, and turbine control set point). The additional information that the TANDEM model requires is the Obukhov length L_obu and the profile of inflow TKE $k^B(z)$, rather than a point TI measurement at hub height. For low TI flows, such as the SBL (TI $\sim 4\%$), knowledge
595 of the vertical $k^B(z)$ profile adds minimal information to the model; running the TANDEM model with only $k^B(z = z_h)$ changes wake centerline predictions by less than 0.4% of U_h. Rather, the significant improvement in wake prediction in the SBL for the TANDEM model, compared with the analytical models, is due to the increased fidelity of physical modeling.

All of the wake models from section 4 are visualized in fig. 9 and fig. 10. In these figures, we visualize yz-slices through the wake for relatively weak stratification ($C_r = 0.1\,\mathrm{K\,h^{-1}}$) and relatively strong stratification($C_r = 0.5\,\mathrm{K\,h^{-1}}$), respectively.

https://doi.org/10.5194/wes-2026-149
Preprint. Discussion started: 27 August 2026

600 Wake cross-sections are shown at three downstream locations. The colorbar is shared across all subplots, with darker contours denoting stronger wakes.

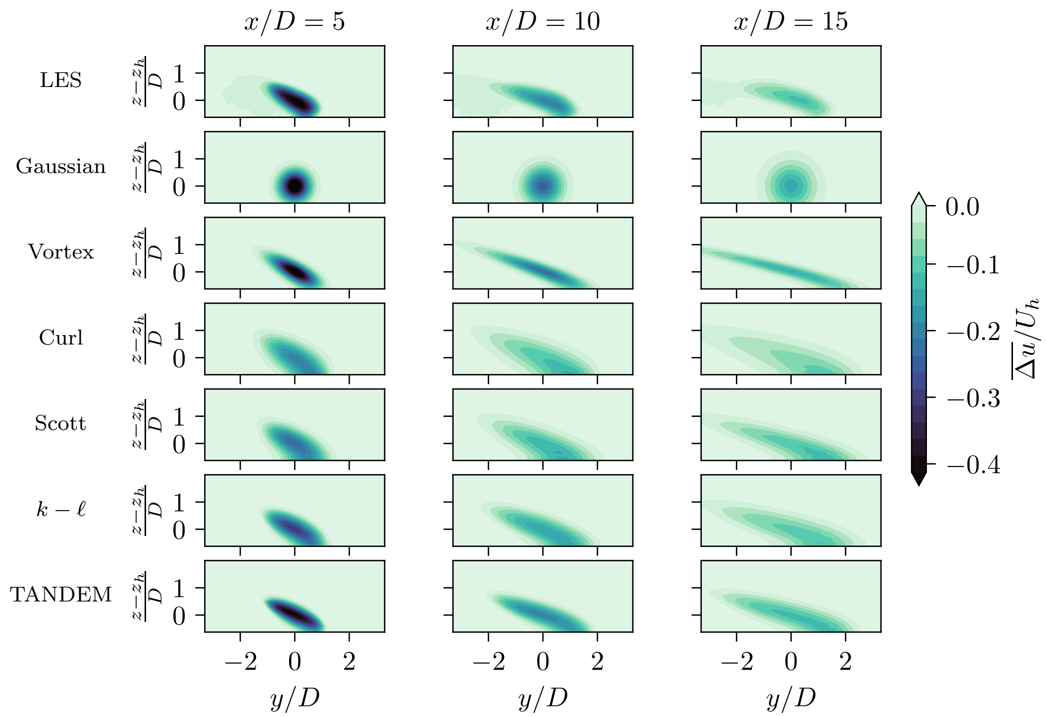

Figure 9. Contour plots of wake velocity deficit at three downstream locations for the inflow cooling rate of $C_r = 0.1\,\mathrm{K\,h^{-1}}$. The reference data is LES, and all of the wake models evaluated in this study are shown: Gaussian, Vortex, Curl, Scott, $k-\ell$, and TANDEM.

In fig. 9, we can see the deficiencies of the analytical models highlighted in section 5.1.1. Specifically, the Gaussian model is axisymmetric in the absence of yaw misalignment, while the Vortex model is overly skewed. However, for the weak stratification case, the velocity magnitudes predicted by the analytical models are reasonably correct, as shown by fig. 8(a). The parabolized RANS models see mixed success. A deficiency of the Curl and Scott models is that at $x/D = 5$, the wake deficit is too weak and diffuse, relative to the LES wake deficit. This is because the Curl and Scott models do not explicitly consider the near-wake region. Instead, the turbulent far-wake begins at the rotor. As a result, the wake recovery begins too rapidly, and wakes are too diffuse downstream. The $k-\ell$ model does include a near-wake region, which improves the wake predictions considerably. Furthermore, the $k-\ell$ model solves the TANDEM equations (with a different eddy viscosity closure) and thus interactions between the turbulence field and the wake deficit field are explicitly modeled. In total, these changes lead to slightly improved predictions for the $k-\ell$ model relative to the Curl and Scott models.

Moving to the strong stratification case, the analytical model predictions begin to degrade. In the analytical models, the maximum wake velocity magnitude is too large due to the incorrect wake spreading rate. Further, the Vortex model is again

https://doi.org/10.5194/wes-2026-149
Preprint. Discussion started: 27 August 2026

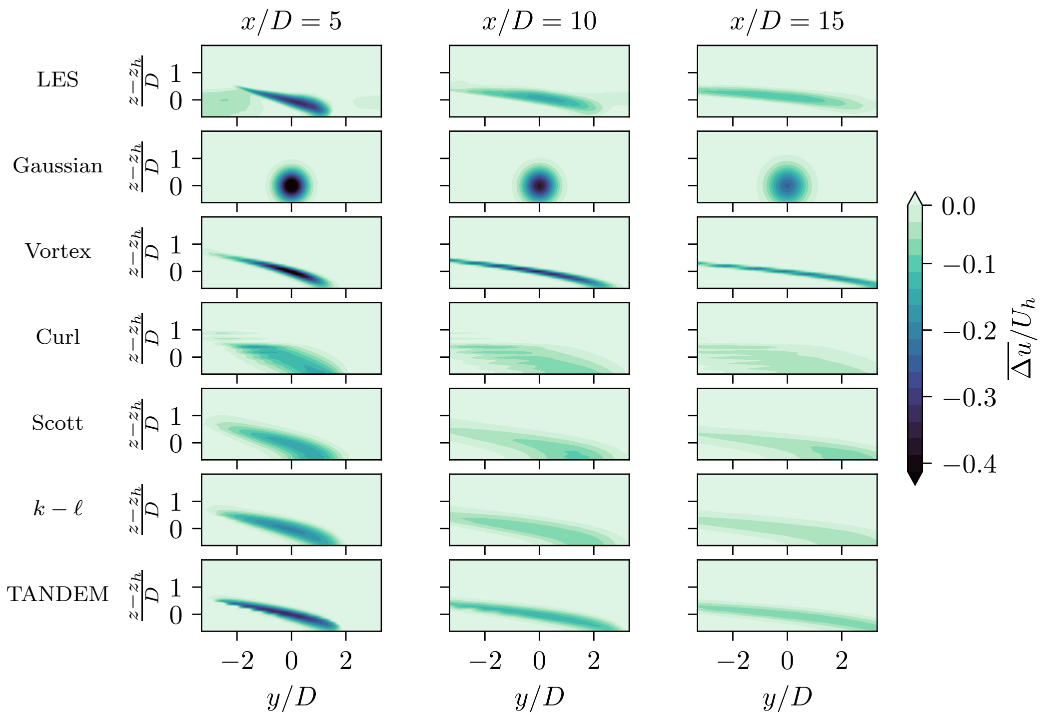

Figure 10. Same as fig. 9 except with $C_r = 0.5\,\mathrm{K\,h^{-1}}$ SBL inflow. Oscillations in the Curl model predictions are due to a change in sign of $\partial U/\partial z$ from the nose of a low-level jet, causing the eddy viscosity to drop to zero at $z - z_h \approx 0.5$ (see section 4.1.1).

too strongly skewed. The parabolized models perform similarly to the weak stratification case. Specifically, the Curl and Scott models are still too diffuse at $x/D = 5$. However, because the wake recovery is relatively faster at $C_r = 0.5\,\mathrm{K\,h^{-1}}$, the discrepancy between the Curl/Scott models and LES is lower. We note that the oscillations in the Curl model predictions are due to a change in sign of $\partial U/\partial z$ from the nose of a low-level jet, causing the eddy viscosity to drop to zero at $z - z_h \approx 0.5$ (see section 4.1.1). The $k-\ell$ model has a slightly different issue: because the mixing length of the $k-\ell$ model is defined by the wake width, the strong wind veer (over 30° across the rotor, see table 2) artificially inflates the mixing length through wake skewing. As a result, the $k-\ell$ model predicts a more rapid wake recovery than what is observed in LES. The TANDEM model excels in predicting the strongly stratified wake for two reasons: (1) the primary mixing length (ℓ_{md}) is linked to the dynamics (shear production and dissipation of Δk) rather than wake geometry, and (2) the surface layer mixing length ℓ_w limits near-surface mixing.

We compare an aggregated error for all of the wake models in fig. 11, which shows the root mean square error in the wake centerline prediction as a function of SBL cooling rate. Errors are averaged over the downstream region $x/D \in [5, 15]$ to focus on the turbulent far-wake. For the TNBL case ($C_r = 0$), all wake models perform approximately equally, with a slight decrease in error for the Gaussian and $k-\ell$ models. Note that in the TNBL, wind veer is small and wakes are nearly axisymmetric.

At $C_r = 0.1\,\mathrm{K\,h^{-1}}$, the performance of the analytical models is still comparable to or better than some of the more complex numerical RANS models. However, the analytical model performance deteriorates as the cooling rate is increased. As shown
630 in fig. 8, the mechanism for the increased error is the incorrect prediction of decreasing wake recovery rate with decreasing inflow TI, due to the neglected wind veer effect.

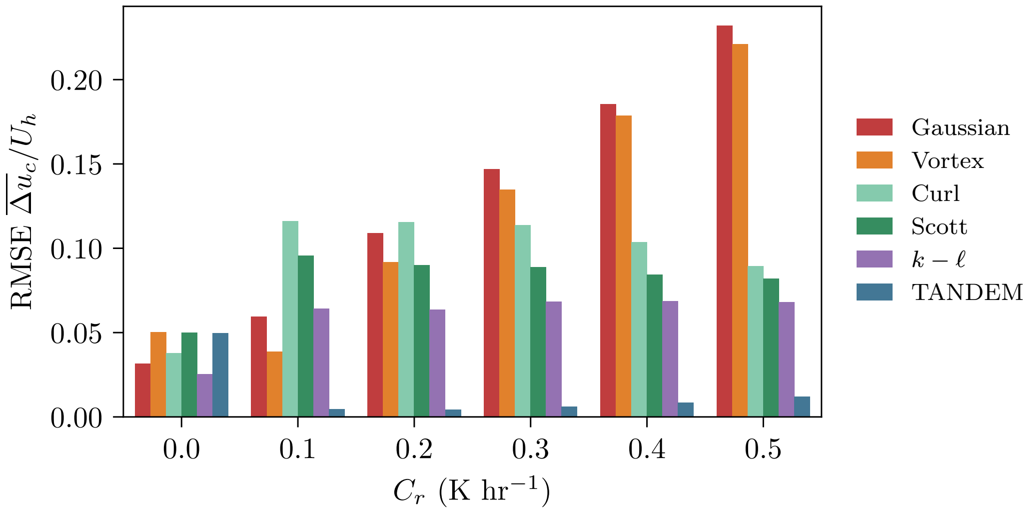

Figure 11. Root mean square error of the centerline wake velocity between wake models and LES, as a function of cooling rate. Errors are averaged over the downstream region $x/D \in [5,15]$.

The TANDEM model performs very well across all ABLs, except for the aforementioned underprediction in wake recovery in the TNBL case. The other parabolized RANS models (Curl, Scott, $k-\ell$) are mixed in their results. Due to the lack of a near-wake region, the Curl and Scott models overestimate wake recovery. As a result, the RMSE exceeds that of the analytical
635 models, particularly at low C_r. As C_r increases, LES wake recovery increases, improving model predictions. The addition of the modeled interaction between $\overline{\Delta u}$ and Δk in the $k-\ell$ model improves model predictions relative to the other parabolized models. However, the geometric mixing length and lack of a near-wall (or buoyancy-driven) secondary mixing scale incur significantly higher error than the TANDEM model for these SBL inflows.

Wake models are often used to estimate power losses of downstream turbines by computing the power of a hypothetical
640 turbine in the wake flow. To estimate the power of a downstream turbine, we assume that the power production (P_{model}) is proportional to the cube of the rotor-averaged, rotor-normal wind speed at a given location. We compare this to the power generated by a hypothetical turbine using the LES flow fields (P_{LES}). In fig. 12, we compute the relative error in P_{model} from P_{LES} at each $x/D \in [5,15]$ in increments of $1D$ and each $y/D \in [-0.5, 0.5]$ (lateral downstream turbine offset) in increments of $0.25D$, totaling 55 ghost turbine points per wake field. The distribution of errors is shown with a box plot separated by
645 cooling rate, with the interquartile range (IQR) denoted by the colored region.

https://doi.org/10.5194/wes-2026-149
Preprint. Discussion started: 27 August 2026

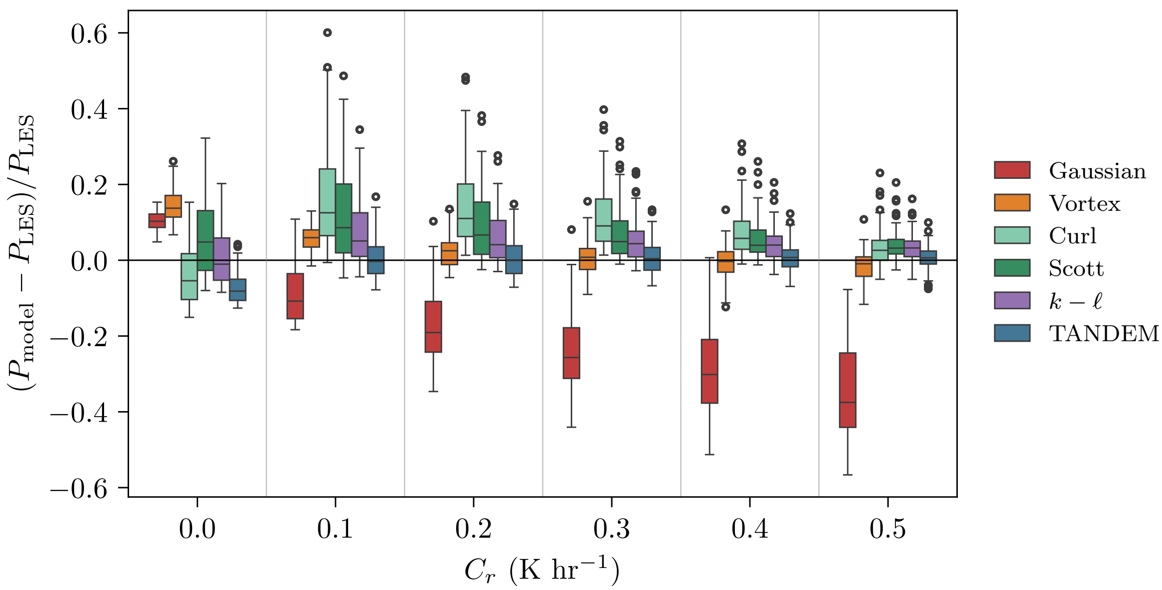

Figure 12. Box plot of error in ghost turbine power prediction between the wake models and LES as a function of SBL cooling rate C_r. Colored box regions denote the interquartile range (IQR), and outlier points lie outside of ±1.5IQR from the median value. For each model and cooling rate, 55 ghost turbines are evenly spaced between $x/D \in [5, 15]$ and $y/D \in [-0.5, 0.5]$.

Figure 12 delivers a practical, quantitative measure for the usefulness of each wake model in the SBL flows. For example, in the least stratified SBL inflow, the Gaussian model predicts most turbine powers within $\pm15\%$, but has a negative bias because the wake spreading coefficient k_w is too small. As cooling rate and stratification increase, the Gaussian model bias becomes monotonically more negative, because the wake spreading rate is decreasing (resulting in stronger modeled wakes) while in the LES data, the wakes are recovering faster and skewing due to veer. Across all ABLs, the MAE of ghost turbine power predicted by the Gaussian model is 21%. On the other hand, the Curl and Scott models overestimate P_{model} because the wakes are too diffuse in the far-wake (MAE: 10.5% and 8.3%, respectively). Power predictions from the Vortex model are generally within $\pm10\%$, and the MAE across all conditions is 5.8%. This is because the overprediction in wake deficit magnitude is compensated for by the overprediction in wake skewing, which effectively advects the wake away from a downstream turbine. The $k-\ell$ model also performs well with low bias across all ABLs (MAE: 6.1%). The TANDEM model performs best across all cooling rates, with nearly zero bias and most power predictions within $\pm5\%$ of the LES truth value (MAE: 4.2%).

To conclude this section, we visualize contours of the wake-added turbulence, Δk. The $k-\ell$ and TANDEM models explicitly solve the coupled equations for both $\overline{\Delta u}$ and Δk, under the hypothesis that explicitly resolving Δk will improve predictions of the wake velocity deficit through more accurate physical modeling. However, the prediction of Δk is also useful, for example, to perform fatigue analysis through load surrogate modeling (Guilloré et al., 2024), but only if the predictions of Δk are

https://doi.org/10.5194/wes-2026-149
Preprint. Discussion started: 27 August 2026

dependable. We compare the predictions of Δk for the $k-\ell$ and TANDEM models to LES data across atmospheric stabilities in fig. 13.

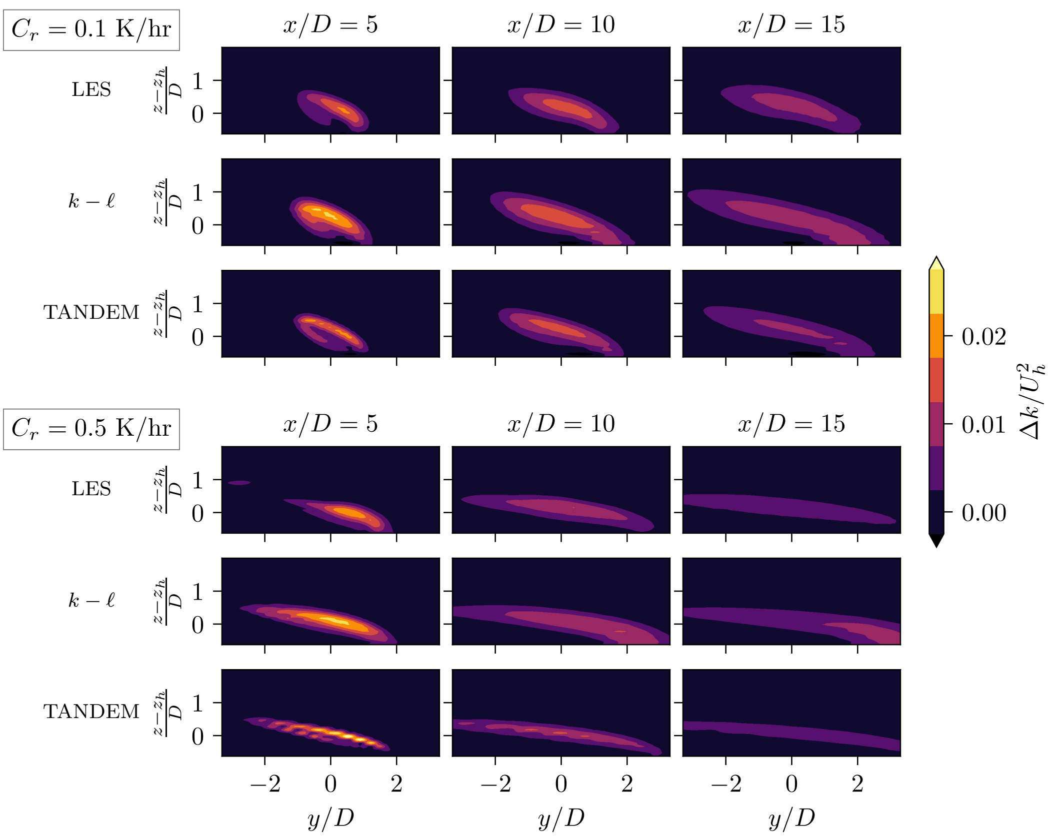

Figure 13. Contour plots of wake-added turbulence at three downstream locations for $C_r = 0.1\,\mathrm{K\,h^{-1}}$ and $C_r = 0.5\,\mathrm{K\,h^{-1}}$. LES data are shown for reference, and the $k-\ell$ and TANDEM model predictions are also shown.

While there are small differences in the Δk predictions between the $k-\ell$ and TANDEM models near the rotor ($x/D = 5$), both model predictions farther downstream show excellent agreement with LES. Near the rotor, the wake-added turbulence is more sensitive to the initial condition (such as σ_{IC}) and near-wake dynamics of the specific models, but the sensitivity to the near-wake handling diminishes downstream. Both model formulations provide reliable predictions of Δk in the SBL for single turbine wakes.

To summarize the single-turbine wake model results, the coupled turbulence and deficit momentum parabolized modeling framework ("TANDEM"), used by the $k-\ell$ and TANDEM models, excels in modeling wakes in stratified ABL conditions. By explicitly modeling the interactions between wake-added turbulence and the velocity deficit, the enhanced mixing due to wind veer without the need for additional calibration parameters. Furthermore, the skewed wake shape in veered conditions is less exaggerated compared with analytical skewed wake corrections, which passively advect the flow with the background flow

https://doi.org/10.5194/wes-2026-149
Preprint. Discussion started: 27 August 2026

direction, due to the coupled turbulence mixing and momentum modeling. As a result, the TANDEM modeling framework (used by the TANDEM and $k-\ell$ models) provides more accurate and reliable predictions of waked turbine power production in the stable ABL than analytical models or parabolized models, which only use a zero-equation eddy viscosity closure.

5.2 Multi-turbine modeling

In this section, we extend the wake model testing to a small, 4-turbine wind farm in a conventionally neutral ABL (CNBL). The CNBL and numerical setup are identical to Heck et al. (2024). A CNBL is initialized with a geostrophic wind speed of $8\,\mathrm{m\,s^{-1}}$ and free atmosphere lapse rate of $1\,\mathrm{K\,km^{-1}}$. The surface roughness is $z_0 = 1\,\mathrm{mm}$ and the latitude is 43.3°, resulting in a power law exponent of approximately 0.11, 2.2° of wind veer across the $100\,\mathrm{m}$-diameter rotor extent, and a turbulence intensity of $\mathrm{TI} \approx 5.5\%$ at hub height ($z_h = 100\,\mathrm{m}$). Four actuator disk-modeled turbines ($C_T' = 4/3$) are placed in the flow with a spacing of $S/D = 6$, and the array is rotated anti-clockwise (as viewed from above) to achieve the desired inflow angle with the turbine rows in four unique simulations.

We wish to investigate how the engineering models perform in multi-turbine arrays. For the parabolic RANS models, downstream turbines are added as an initial velocity deficit at the rotor plane, which restarts the forward-marching numerical solution. Turbine power in LES and in the wake models is computed as $P = -\boldsymbol{F_T} \cdot \boldsymbol{u}_d$, where $\boldsymbol{u}_d$ is the rotor-averaged velocity vector at the location of the turbine (i.e., modified by the turbine induction a_n). In the wake models, the rotor-averaged velocity is computed using momentum theory such that $|\boldsymbol{u}_d| = U_{\mathrm{REWS}} \cos(\gamma)(1-a_n(\gamma))$, where U_{REWS} is the rotor-equivalent velocity normal to and averaged over the turbine face, which may include the wakes of upstream turbines. Therefore, the modeled power can be written

$$P = \frac{1}{2}\rho A_d C_T' U_{\mathrm{REWS}}^3 \cos^3(\gamma)(1-a_n(\gamma))^3. \tag{32}$$

For all model power predictions in this section and in section 5.3, the Unified Momentum Model is used to compute a_n from the turbine set point inputs C_T' and γ, rather than relying on an empirical cosine power-yaw relationship (Gebraad et al., 2016; Liew et al., 2020). LES and model-predicted turbine power are shown in fig. 14.

The lowest array-averaged power output occurs in the fully aligned wind direction (fig. 14(a), 0°), and power monotonically increases as lateral turbine spacing increases (wake interactions decrease). The analytical Gaussian model (Bastankhah and Porté-Agel, 2016) accurately captures the waked turbine power without further model calibration to the superposition model and wake spreading parameterization from Niayifar and Porté-Agel (2016) and the wake-added TI model from Crespo and Hernández (1996). The accurate Gaussian model power predictions in the CNBL are corroborated by previous work, given that the empirical coefficients in the parameterizations from the Gaussian model and necessary sub-models are tuned to neutrally stratified boundary layers. Furthermore, the wind veer in the CNBL is small, so the wake deficits retain an approximately axisymmetric Gaussian shape. The Curl and Scott models yield the highest predictive error, overestimating the wake recovery throughout the wind farm, particularly for the second row turbine. The $k-\ell$ model slightly overpredicts the power produced by the second row turbine, primarily due to the faster wake recovery from the difference in near-wake handling (e.g., fig. 9), but predicts similar power production to the Gaussian model in the third and fourth rows. The TANDEM model performs ex-

https://doi.org/10.5194/wes-2026-149
Preprint. Discussion started: 27 August 2026

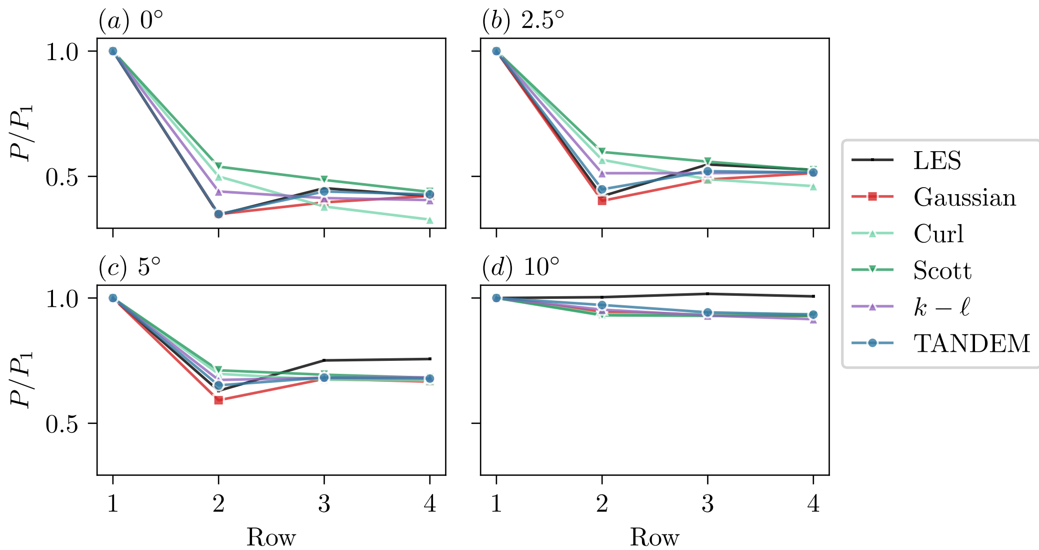

Figure 14. Power production, normalized to the power produced by the leading row turbine (P_1), for a 4-turbine array at (a) 0°, fully-aligned with the incident wind, (b) 2.5°, (c) 5°, and (d) 10°, where turbines are separated by $S_y \approx 1D$ of lateral spacing. LES-measured power is in the black lines, and model predictions are in the colored markers.

ceptionally well, yielding the lowest error among the three models. Notably, the TANDEM and $k-\ell$ models have no empirical coefficients that have been calibrated to multi-turbine wind farms; all model parameters were calibrated in section 3 to single-turbine wakes. All models perform best in fully-aligned or near fully-aligned conditions (fig. 14(a,b)), degrading slightly in the partial wakes. This is likely due to flow acceleration around the sides of upstream turbines, which is not accounted for in any of the engineering models presented here (c.f. Gribben and Hawkes, 2019).

While the modeled turbine power only depends on the modeled velocity deficit field $\overline{\Delta u}$, comparing the modeled Δk can lend insight into understanding the physical mechanisms underlying the modeled power predictions. In fig. 15, we show the LES and modeled wake-added turbulence, integrated in the yz-plane and shown as a function of streamwise position, for each array orientation. The profiles of integrated Δk show that the uptick in LES turbine power after the second row is accompanied by elevated levels of mixing due to the additional wake-added turbulence from the leading turbine wake. The analytical models approximate this behavior with the parameterized wake spreading relation $k_w(\mathrm{TI})$ coupled with an empirical wake-added TI expression (c.f. Niayifar and Porté-Agel, 2016).

By contrast, the TANDEM model reproduces this non-monotonic trend in row-wise power generation by faithfully capturing the dynamics of the wake-added turbulence. The $k-\ell$ model also produces similar trends in the evolution of wake-added turbulence through the array, with larger quantitative deviations from the LES. These deviations grow in the partial overlap wakes because the definition of a "wake-width," used to define the mixing length in the $k-\ell$ model, becomes ill-posed. Instead, the wake-width is the width of multiple wakes in superposition, which increases ℓ, ν_T, and therefore shear production of Δk.

https://doi.org/10.5194/wes-2026-149
Preprint. Discussion started: 27 August 2026

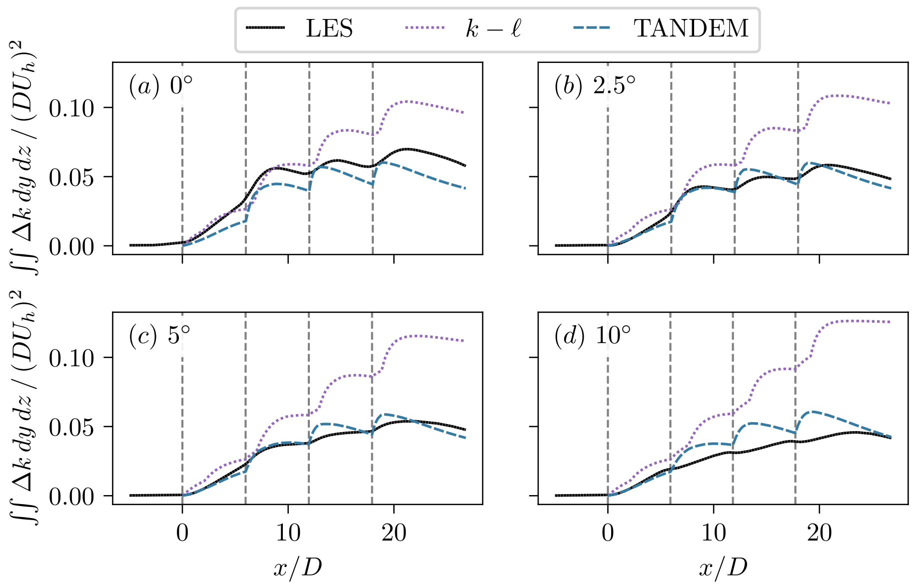

Figure 15. Streamwise evolution of wake-added turbulence, integrated over the computational yz-domain, for a 4-turbine array at (a) 0°, (b) 2.5°, (c) 5°, and (d) 10°. LES predictions are given by the solid black line, while model predictions are shown in the dotted ($k-\ell$) and dashed (TANDEM) lines.

The Curl and Scott models overestimate array power production due to the overestimation in wake recovery from the missing near-wake dynamics, and do not produce the non-monotonic trend in power because of the missing feedback with Δk shown in fig. 15.

To summarize, the TANDEM model, calibrated only with single-turbine model parameters, provides exceptional predictions of a small four-turbine wind farm in conventionally neutral ABL conditions. The non-monotonicity in row-wise power production is predicted by the TANDEM model because the evolution of the wake-added turbulence is well captured by the coupled Δk–$\overline{\Delta u}$ dynamics. The parabolic RANS models that do not co-evolve a wake-added turbulence field (Curl and Scott models) predict monotonically decreasing turbine power production moving downstream. Therefore, the co-evolution of the turbulence and deficit momentum fields in the parabolized RANS framework captures critical physical interactions for wind plant flows that are missing without the turbulence coupling.

5.3 Wake steering control case study

In this section, we test the wake models in a wake steering application, where upstream wind turbines are intentionally yaw-misaligned to redirect their wakes away from downstream turbines (Gebraad et al., 2016). However, Gaussian-based models poorly capture the curled wake shape downstream of yaw-misaligned turbines, hindering robust controller implementation. Here, we use LES of a 5×5 wind farm array immersed in a conventionally neutral ABL. The turbine layout and ABL inflow

https://doi.org/10.5194/wes-2026-149
Preprint. Discussion started: 27 August 2026

are identical to the 25-turbine wind farm setup in Heck et al. (2025). To summarize, the CNBL is initialized with a geostrophic wind speed of $G = 10\,\mathrm{m\,s^{-1}}$ and surface roughness $z_0 = 1\,\mathrm{mm}$. The latitude is $43.3°$ and the free atmosphere lapse rate is $3\,\mathrm{K\,km^{-1}}$. The resulting CNBL has a power law exponent of approximately 0.11, freestream $\mathrm{TI} \approx 5.6\%$, and $1.9°$ of wind veer across the $100\,\mathrm{m}$-diameter rotor. The array consists of 25 actuator disk-modeled turbines and is rotated $42.5°$ from the inflow to create a diamond-shaped layout with partial wake overlap.

Next, we run two simulations using the same wind farm layout and ABL inflow to assess the efficacy of wake steering (static yaw control) on the wind farm power production. In the baseline case, termed Greedy control, all 25 turbines operate at the Betz optimum: $C_T' = 2$ (corresponding to $C_T = 8/9$) and $\gamma = 0°$. In a second LES case, termed Wake steering, all turbines still operate at a local thrust coefficient of $C_T' = 2$, but upstream turbines are yaw misaligned with the incoming flow. Here, we adopt a simple yaw set point heuristic: the leading row turbines yaw misalign by $-30°$, and each subsequent downstream row adopts half the yaw misalignment of the previous row ($-15°$; $-7.5°$; $-3.75°$). Due to the partial wake, negative yaw angles are favorable to positive yaws. The final row of wind turbines operates at the Betz optimum set point ($C_T' = 2.0$) and is therefore yaw-aligned in all columns. Because actuator disk LES is well-known to predict turbine power production that exceeds the Betz limit (Shapiro et al., 2019), we report mean turbine power production normalized by P_{Betz}. In the LES data, we compute P_{Betz} as the mean power production of the first-row turbines in the Greedy control case operating in freestream conditions. Each wake model is prescribed the mean inflow profiles and properties from the precursor LES simulation and given the array layout and turbine set points. The wind farm flow models are used to estimate the turbine-level power production, which is also normalized by P_{Betz} computed in the same manner. Correlation plots for the turbine-level normalized power between the models and LES are shown in fig. 16.

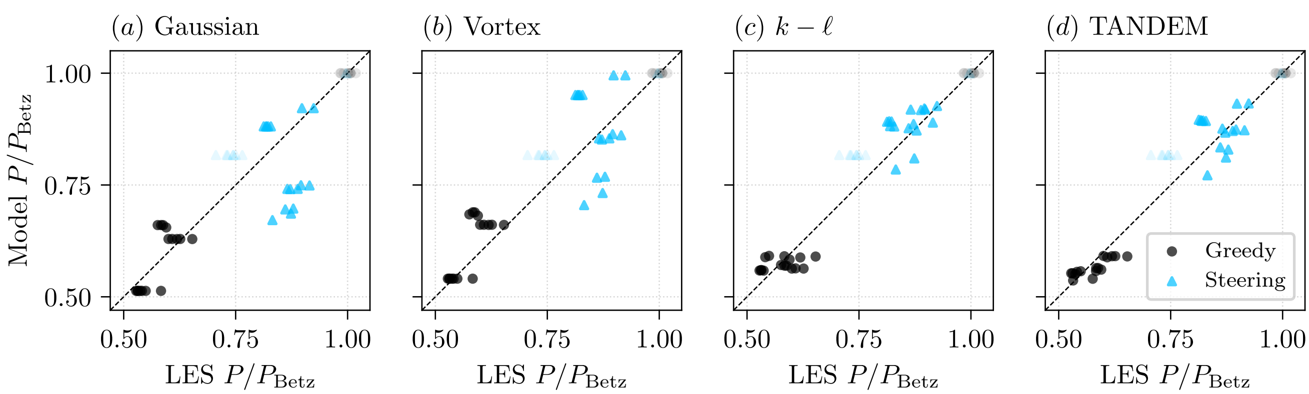

Figure 16. Scatter plots of normalized power from various wake models compared with the power from LES fora 25-turbine wind farm. Greedy control points are shown in black, while wake steering predictions are shown in blue. Freestream turbine powers are shown in higher transparency.

We evaluate the wake model predictions for four wake models: Gaussian, Vortex, $k-\ell$, and TANDEM. In Greedy control, shown in fig. 16, all wake models predict normalized, turbine-level power production accurately, deviating by less than 4% of

https://doi.org/10.5194/wes-2026-149
Preprint. Discussion started: 27 August 2026

P_{Betz} in MAE (error analysis shown in table 3). The strong model performance of all models is corroborated by section 5.2, which investigated a smaller four-turbine array of yaw-aligned turbines in a similar CNBL. That is, empirically calibrated analytical models accurately predict wake interactions in yaw-aligned operation. In these models, there is a small benefit to the numerical $k-\ell$ and TANDEM models. Conversely, in Wake steering control, shown in fig. 16, the Gaussian model drops considerably in predictive accuracy, with a three-fold increase in MAE of turbine-level power prediction relative to Greedy control. The analytical Vortex model (fig. 16(b)), which approximates the curled wake shape with an analytical form, performs slightly better than the Gaussian model, but still doubles in MAE. However, the parabolic RANS models (fig. 16(c, d)) perform the best, with MAE computed across waked turbines around 5% of P_{Betz} while retaining high correlation with the LES data.

Table 3. Errors between wake model predictions and LES of normalized power production, P/P_{Betz}. Mean absolute error (MAE) is computed with all turbines ($N = 25$) as well as for waked turbines only ($N = 16$). Correlation is computed as the Pearson correlation coefficient, and $\mathcal{R}^2$ is the coefficient of determination.

Case	Model	MAE	MAE (waked only)	Bias	Bias (waked only)	Correlation	R^2
	Gauss	0.027	0.037	0.005	0.008	0.98	0.97
Greedy	Vortex	0.031	0.043	0.023	0.036	0.98	0.95
control	$k-\ell$	0.023	0.031	-0.003	-0.005	0.99	0.98
	TANDEM	0.018	0.024	-0.008	-0.013	0.99	0.99
	Gauss	0.092	0.109	-0.021	-0.068	0.22	-0.91
Wake	Vortex	0.080	0.091	0.030	0.012	0.45	-0.38
steering	$k-\ell$	0.048	0.040	0.036	0.022	0.84	0.47
	TANDEM	0.051	0.044	0.027	0.008	0.74	0.42

In fig. 17, we investigate the structural error of the turbine-level power predictions, averaged as a function of wind farm row. Greedy control is shown first in fig. 17(a). By definition of the chosen normalization (P_{Betz}), the leading row Greedy control turbines incur zero error. Moving downstream, error grows substantially in both the Gaussian and Vortex models, which tend to overpredict power in the interior rows of the farm. By contrast, the $k-\ell$ and TANDEM model errors are non-monotonic and, on average, lower in magnitude.

Moving to the Wake steering case (fig. 17(b)), we see that all wake models incur greater errors in predicted power. The leading row error is the same across all wake models because all wake models use the calibration-free UMM to predict the power. The UMM incurs some model error in predicting the leading-row power because wind shear, wind veer, and freestream turbulence in the ABL are not accounted for in the UMM derivation (Heck et al., 2026). Future work should extend physics-based model predictions of rotors to ABL inflows with yaw misalignment. The second-row turbine power is overestimated in all wake models, in part due to errors in estimating the power of the yaw-misaligned second-row turbines, which is similar to the freestream turbines. This overestimation is highest in the Vortex model because the wake deflection and curling are overestimated relative to LES. Deeper into the farm, the Gaussian model drastically underpredicts power generation because it does not capture the curled wake shape or cumulative curl effects. The Vortex model also underpredicts power due to missing

https://doi.org/10.5194/wes-2026-149
Preprint. Discussion started: 27 August 2026

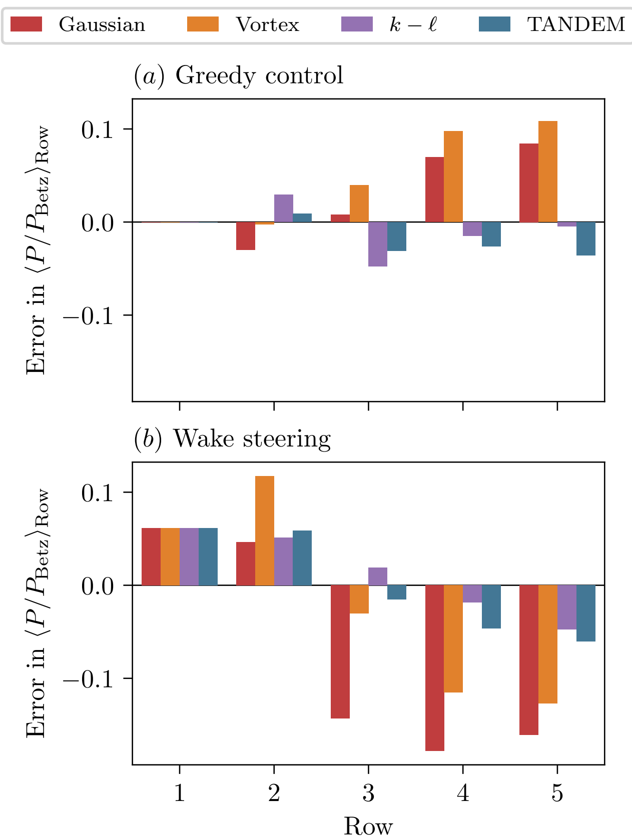

Figure 17. Error in model predictions for normalized power P/P_{Betz}, averaged as a function of wind turbine row. Row 1 turbines see freestream ABL inflow. (a) Greedy control. (b) Wake steering control.

cumulative curl effects in Rows 4–5. Relative to the analytical models, the $k-\ell$ and TANDEM model power predictions incur less than half the error past the third row of turbines, due to the direct modeling of the cumulative wakes and wake-added TKE, as well as the modeled secondary steering effects of yaw misalignment (Bay et al., 2023).

Finally, we show the aggregated wind farm power production and compute the predicted gain yielded by Wake steering. The farm-averaged normalized power is computed by averaging the normalized power of each turbine for each control strategy. Farm-averaged power is shown in fig. 18(a). Then, in fig. 18(b), the relative difference in power production between Wake steering and Greedy control is computed and expressed as a percent. Predictions for the power gain in wake steering are also shown for each wake model.

In the Greedy control strategy, all wake models predict the mean normalized farm power within 1.2%, except for the Vortex model, which has a slight overestimation of power of $+3.2\%$. Simply put, power estimates for a yaw-aligned wind turbine array are excellent using all four models. In the Wake steering case, models incur slightly higher errors, reflecting fig. 17(b).

https://doi.org/10.5194/wes-2026-149
Preprint. Discussion started: 27 August 2026

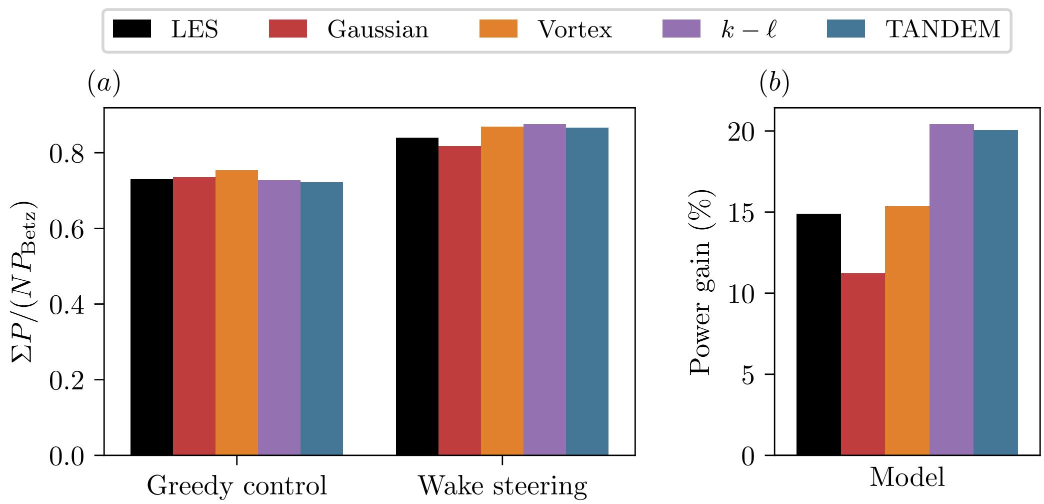

Figure 18. (a) Farm-averaged normalized power, computed with LES and various wake models, under greedy control and wake steering control strategies. (b) Power gain from wake steering control in LES and predicted by various wake models.

The Gaussian model underpredicts the power under Wake steering by approximately -3.5%, relative to LES farm power, due to drastic underprediction of power in the interior rows of the farm. As a result, the potential power gain is also underestimated. By contrast, the Vortex ($+3.6\%$), $k-\ell$ ($+4.3\%$), and TANDEM ($+3.3\%$) models slightly overestimate the predicted power in wake steering control, particularly in the leading row of turbines (see fig. 17). These three models also overpredict the realized power gain due to wake steering, due to slight underpredictions of Greedy control farm power and overpredictions in Wake steering control. The Vortex model is slightly overestimated by the same amount in both cases, and therefore predicts an overall power gain closest to the actual LES power gain of 14.9%.

There are several sources of error that likely compound in the turbine- and farm-level power comparisons presented here. First, some error is incurred in modeling the power-yaw relationship in sheared ABL inflows, as shown in fig. 17(b). Errors in turbine power prediction are further exacerbated by array-scale blockage (Gribben and Hawkes, 2019). Additionally, the decay of yaw-induced counter-rotating macrovortices is not included in the models presented in this study for simplicity (Shapiro et al., 2020). Finally, the influence of wind shear and wind veer (Heck et al., 2026), freestream turbulence (Revaz and Porté-Agel, 2025), and other ABL parameters is not captured by existing rotor models, which can induce substantial deviations in power extraction efficiency and induction from uniform flow assumptions. Despite these limitations, the parabolized RANS models (TANDEM and $k-\ell$) show promise for enabling wake steering control and, more generally, collective control strategies through improved prediction of turbine-level power generation in the LES cases simulated here.

https://doi.org/10.5194/wes-2026-149
Preprint. Discussion started: 27 August 2026

5.4 Deep-array challenges and future work

In this final results section, we show the asymptotic behavior of several wake models and highlight opportunities for future work. Using the CNBL precursor flow from section 5.2, we perform an additional simulation of a 10-row wind farm that is fully aligned with the incident ABL inflow (Wind direction 0°). To elongate the computational domain, the precursor flow is tiled by a factor of two (Sanchez Gomez et al., 2023). All of the turbines, which are evenly spaced $S/D = 6$ apart, operate in yaw alignment at $C_T' = 4/3$.

The 10-turbine wind farm elucidates the asymptotic behavior of the different wake models. Power generation as a function of row number is shown in fig. 19(a). The first four rows of the new 10-turbine wind farm are nearly identical to the 0°-aligned four-turbine farm from section 5.2. Therefore, in the first few rows, the TANDEM model predictions are excellent. After the fifth row of turbines, however, the TANDEM model and the LES lines begin to diverge. While the LES turbine power becomes approximately constant, matching the approximate asymptote reached in the analytical Gaussian model and parabolic $k-\ell$ model, the TANDEM model turbine power begins to decline, deviating from the LES reference behavior.

To illustrate the dependence of the Gaussian model predictions on empirical superposition sub-models, fig. 19 also includes two Gaussian model variants based on plausible changes to the cumulative-wake treatment. The first replaces the modified linear superposition method with freestream linear superposition ("FLS"; Lissaman, 1979). The second retains modified linear superposition but disables the empirical wake-added-turbulence contribution, such that the wake-expansion coefficient depends only on the background turbulence, $k_w = k_w(\mathrm{TI}^B)$ ("no WATI"). Both changes substantially alter the cumulative power prediction. Consequently, the Gaussian model predictions for the power in cumulative wakes are not a consequence of a modeled farm-scale momentum or energy exchange, nor of inherent accuracy in the Gaussian turbine-wake representation. Rather, the model predictions depend strongly on the selected wake-superposition and wake-added-turbulence closures. These closures can produce a compelling prediction of turbine power in cumulative wakes, but they do not explicitly represent the vertical entrainment of momentum from the atmospheric boundary layer that sustains power production in large wind farms and are instead empirically tuned for a narrow range of ABL conditions (Stevens et al., 2016; Lanzilao and Meyers, 2024; Kirby et al., 2025; Aerts et al., 2026). The comparison therefore should not be interpreted as evidence that the Gaussian wake formulation independently captures the governing array-scale physics.

The drop in the TANDEM model turbine power production is associated with an increase in the centerline wake velocity magnitude, shown in fig. 19(b). In the deep rows of the farm, the TANDEM model wake recovery appears to slow, relative to the upstream rows. In conjunction, for the TANDEM model, the wake-added turbulence Δk plateaus after the fifth row, shown in fig. 19(c). In contrast, the wake recovery in the $k-\ell$ model is enhanced moving deeper into the farm. This enhanced wake recovery is explained by the continuously increasing levels of wake-added turbulence in the $k-\ell$ model. The wake-added turbulence also increases with increasing rows in the LES data, albeit at a slower pace than the $k-\ell$ model.

The asymptotic behavior of the TANDEM model is likely caused by a feedback loop where the wake-added turbulence is overly dissipative deep into the turbine array, compared with LES $\Delta\varepsilon$. As a result, Δk decreases, and therefore ℓ_{md} decreases (see numerator, eq. (10)). But a drop in ℓ_{md} results in a drop in ν_T, which scales the shear production term. So a nudge from

https://doi.org/10.5194/wes-2026-149
Preprint. Discussion started: 27 August 2026

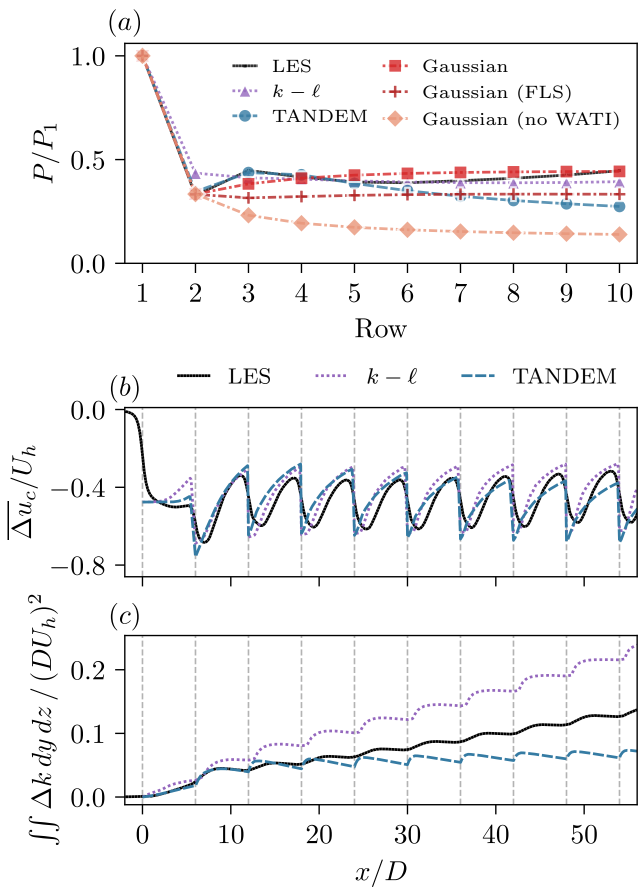

Figure 19. Turbine and wake quantities for a 10-turbine array fully aligned in CNBL inflow conditions. For all subfigures, LES results are in black, and wake models are denoted by the following styles: red dash-dot (Gaussian and variants); purple dotted ($k-\ell$); blue dashed (TANDEM). (a) Turbine power production, normalized to the leading turbine power production, as a function of row number. (b) Centerline wake velocity as a function of streamwise distance. (c) Wake-added turbulence, integrated in the yz-plane as a function of streamwise distance.

the equilibrium dissipation causes a cascading response that prevents further growth of Δk. Future work should explore two-equation closures in a computationally efficient, parabolized form, such as the popular $k-\varepsilon$ or $k-\omega$ RANS models. Explicitly modeling the evolution of the dissipation of wake-added TKE would likely add key physics to better model the asymptotic deep-array behavior observed in fig. 19. Additionally, future work should couple the parabolized RANS models with a top-down, physics-based ABL model (Stevens et al., 2016) to include the feedback with the large-scale ABL evolution due to the presence of the wind farm.

https://doi.org/10.5194/wes-2026-149
Preprint. Discussion started: 27 August 2026

6 Conclusions

In this study, we propose a novel wake modeling approach that extends the work of Klemmer and Howland (2025). The key insight of the proposed wake model is to co-evolve a parabolic prognostic equation for the wake-added turbulence kinetic energy (TKE) Δk with the streamwise momentum deficit $\overline{\Delta u}$. We term this approach the Turbulence ANd DEficit Momentum (TANDEM) wake model framework. By co-evolving the wake velocity, which generates wake-added TKE through shear production, with the evolution of the wake-added turbulence, which acts to mix and diffuse the wake, the TANDEM model is a versatile model that can be applied to a wide range of atmospheric conditions, turbine control strategies, and wind farm layouts with minimal calibration.

The TANDEM model uses a generalized mixing length eddy viscosity closure that chooses between the minimum of two candidate mixing lengths. The first driving mixing length in the eddy viscosity formulation is a minimum dissipation mixing length ℓ_{md}, which serves as a constrained minimization of the dissipation of wake-added turbulence. Derived based on the flow dynamics (balance of shear production and dissipation) rather than geometry (such as the wake half-width), the minimum dissipation mixing length ℓ_{md} shows excellent robustness to veered inflow conditions and in wake merging/superposition. The second mixing length is a Monin–Obukhov surface layer length scale, which suppresses flow mixing in stratified conditions near the wall. The TANDEM model quantitatively captures the increase in wake recovery rate due to inflow wind veer. Compared with five other popular wake models, the TANDEM model has the lowest predictive error in estimating the power production of a waked downstream turbine across five stratified ABLs, with a mean absolute error over 25% lower than the next best wake model and nearly 80% lower than a Gaussian model. We also demonstrate that the coupled momentum–turbulence modeling excels at modeling the superimposed wakes within small wind turbine arrays and, along with the $k-\ell$ model, predicts turbine-level power production in a wake steering case with higher accuracy (lower MAE) than the Vortex sheet model.

Still, the TANDEM model can be improved in future work. In particular, array-level effects are completely neglected in the current modeling framework. Additionally, the cumulative wakes deep within a wind farm are not well modeled due to the evolution of the dissipation of wake-added TKE. An extension to a parabolized $k-\epsilon$ or $k-\omega$ would likely improve the wake model robustness to deep array effects. Physics-based coupling with a top-down ABL model would also likely improve model predictions. Finally, it is unclear whether the current approach could be used to model wind farm wakes, or if additional dynamics (such as the lateral momentum equation) would need to be explicitly included.

Appendix A: Large-eddy simulation numerical details

A1 Synthetic turbulent inflow LES

A synthetic turbulent inflow LES method, introduced by Heck and Howland (2026), is used to prescribe controlled inflow conditions for a single turbine wake. Three domains are run concurrently: (1) primary domain with an actuator disk-modeled wind turbine, (2) empty domain of identical dimensions to the primary domain, and (3) a shortened domain used to sustain forced, homogeneous, isotropic turbulence (HIT). Turbulence is generated from the HIT simulation, and fluctuations are imposed on

https://doi.org/10.5194/wes-2026-149
Preprint. Discussion started: 27 August 2026

the fringe targets in the primary and empty domains. A high-pass filter of $\lambda_{\text{HP}} = 2\pi D/3$ is used to limit the large length scales of turbulence. A proportional-integral TI controller is used to set the turbulence level at the rotor. For all simulations, the primary and empty domain sizes are $(L_x, L_y, L_z) = (10\pi D, 4\pi D, 2\pi D)$, and each is discretized into $480 \times 192 \times 96$ points. Slip walls are prescribed on the top and bottom surfaces. The turbine is centered laterally in the domain and placed $x = 5D$ downstream to accommodate the induction region upstream of the turbine. Flow statistics are averaged over 24 flow-through times, which is sufficient for convergence (Heck and Howland, 2026).

A2 Concurrent-precursor simulations

The concurrent-precursor method (Stevens et al., 2014) is used to perform LES of single turbines and wind farms in neutrally and stably stratified ABL flows. First, we introduce the numerical details used for the single-turbine ABL LES. We use the methodology used in Shen et al. (2024) to initialize a nocturnal stable ABL, where the surface cooling rate C_r (in $\mathrm{K\,h^{-1}}$) is prescribed on the bottom boundary, and the free atmosphere is neutrally stratified. In the limit of $C_r \to 0$, the boundary layer becomes the turbulent Ekman layer and is initialized as isothermal. The free atmosphere temperature and initial ground temperature are set to $300\,\mathrm{K}$. The cooling rate C_r and surface roughness z_0 are varied throughout the simulations to alter the structure of the ABL. The latitude is fixed at $45°$, and the geostrophic wind speed is $G = 12\,\mathrm{m\,s^{-1}}$. The turbine shares the dimensions of the IEA 15 MW reference turbine ($240\,\mathrm{m}$ rotor diameter and $150\,\mathrm{m}$ hub height) and is centered laterally in the domain. For all SBL simulations ($C_r > 0$), the domain size is $(7.68\,\mathrm{km} \times 3.2\,\mathrm{km} \times 1.6\,\mathrm{km})$ with a grid resolution of $(20\,\mathrm{m} \times 12.5\,\mathrm{m} \times 6.25\,\mathrm{m})$ in the streamwise, lateral, and wall-normal directions, respectively (same as Heck and Howland (2026)). After $10\,\mathrm{h}$, the domain is rotated to align the hub-height flow with the x-direction. Flow statistics are time-averaged between 13–$20\,\mathrm{h}$. Inflow statistics for the LES cases used in the TANDEM model calibration (see section 3.2) are given in section A2. For all TNBL simulations ($C_r = 0$), the vertical domain size is quadrupled to accommodate boundary layer growth ($L_z = 6.4\,\mathrm{km}$) and the vertical grid resolution is doubled to $12.5\,\mathrm{m}$, which is still sufficient for resolving the rotor-scale turbulence in neutrally stratified ABLs (Heck and Howland, 2025).

Table A1. Summary of SBL simulations used in the TANDEM model calibration. Simulations share a surface roughness of $z_0 = 1\,\mathrm{cm}$, geostrophic wind speed of $G = 12\,\mathrm{m\,s^{-1}}$, and latitude of $\phi = 45°$.

C_r ($\mathrm{K\,h^{-1}}$)	U_h ($\mathrm{m\,s^{-1}}$)	Power law exp.	Veer α_v (deg)	ψ_h (deg)	$u_\star$ ($\mathrm{m\,s^{-1}}$)	L_{obu} (m)	TI (%)	L_0^x (m)	L_0^y (m)
0.3	11.2	0.32	24.6	-2.3	0.35	133	3	40	16
0.5	12	0.36	37.2	-3.5	0.32	75	2.3	33	14

Next, we consider the wind farm simulations. All wind farm simulations are performed in the conventionally neutral boundary layer (CNBL) and use the same CNBL inflows as Heck et al. (2025). The CNBL is initialized using a constant lapse rate throughout the entire domain, following Liu et al. (2021). We spin up the CNBL for $40\,\mathrm{h}$ to allow inertial oscillations to decay (Liu et al., 2021; Heck and Howland, 2025). Then, a short domain rotation is performed to align the hub-height flow with the x-direction, and a wind farm is immersed in the CNBL to compute flow statistics. For all wind farm simulations,

https://doi.org/10.5194/wes-2026-149
Preprint. Discussion started: 27 August 2026

we use a $100\,\mathrm{m}$-diameter turbine with hub height $z_h = 100\,\mathrm{m}$. The surface roughness is $1\,\mathrm{mm}$ in the wind farm simulations, and zero heat flux is imposed as a bottom boundary condition. For the four-turbine wind farm (section 5.2), the domain size is $3.84\,\mathrm{km} \times 1.28\,\mathrm{km} \times 1.28\,\mathrm{km}$ and the grid resolution is $10\,\mathrm{m} \times 5\,\mathrm{m} \times 5\,\mathrm{m}$. The geostrophic wind speed is set to $G = 8\,\mathrm{m\,s^{-1}}$ and the free atmosphere lapse rate is $1\,\mathrm{K\,km^{-1}}$. Flow statistics are time-averaged for two hours (approximately 13 flow-through times at hub height). Additionally, the same CNBL used in the four-turbine wind farm is tiled twice in the streamwise direction (Sanchez Gomez et al., 2023) to investigate the ten-row wind farm case shown in section 5.4. For the 10-row wind farm, the time averaging is increased to four hours. For the 25-turbine wind farm (section 5.3), the domain size is $18.4\,\mathrm{km} \times 9.2\,\mathrm{km} \times 1.5\,\mathrm{km}$ and the grid resolution is $24\,\mathrm{m} \times 12\,\mathrm{m} \times 6\,\mathrm{m}$. The geostrophic wind speed is $G = 10\,\mathrm{m\,s^{-1}}$ and a stronger free atmosphere lapse rate of $3\,\mathrm{K\,km^{-1}}$ is used to mitigate CNBL growth. Flow statistics are time-averaged for four hours (approximately 6 flow-through times).

Appendix B: Unified Momentum Model

The Unified Momentum Model (UMM) is an extension of classical momentum theory introduced by Liew et al. (2024) to enable induction, thrust, and power predictions at high thrust coefficients and nonzero yaw misalignments. The model is solved through fixed-point iteration of five coupled, nonlinear equations, given the local thrust coefficient $C_T' = 2|\boldsymbol{F}_T|/(\rho A_d u_d^2)$ and yaw misalignment at hub-height, γ. Here, $\boldsymbol{F}_T$ is the thrust imparted on the flow by the rotor, A_d is the rotor swept area, ρ is the fluid density, and u_d is the rotor-normal, rotor-averaged velocity.

$$a_n = 1 - \sqrt{\frac{u_\infty^2 - u_4^2 - v_4^2}{C_T' \cos^2(\gamma) u_\infty^2} - \frac{(p_4 - p_1)}{\frac{1}{2}\rho C_T' \cos^2(\gamma) u_\infty^2}} \tag{B1}$$

$$u_4 = -\frac{1}{4} C_T' (1 - a_n) \cos^2(\gamma) u_\infty + \frac{u_\infty}{2} + \frac{1}{2}\sqrt{\left(\frac{1}{2} C_T' (1 - a_n) \cos^2(\gamma) u_\infty - u_\infty\right)^2 - \frac{4(p_4 - p_1)}{\rho}} \tag{B2}$$

$$v_4 = -\frac{1}{4} C_T' (1 - a_n)^2 \sin(\gamma) \cos^2(\gamma) u_\infty \tag{B3}$$

$$\frac{x_0}{D} = \frac{\cos(\gamma)}{2\beta} \frac{u_\infty + u_4}{|u_\infty - u_4|} \sqrt{\frac{(1 - a_n)\cos(\gamma) u_\infty}{u_\infty + u_4}} \tag{B4}$$

$$p_4 - p_1 = -\frac{1}{2\pi} \rho C_T' (1 - a_n)^2 \cos^2(\gamma) u_\infty^2 \arctan\left[\frac{1}{2}\frac{D}{x_0}\right] + p^{\mathrm{NL}}(C_T', \gamma, a_n, x_0). \tag{B5}$$

We assume $u_\infty = U_{\mathrm{REWS}}$ when applying the UMM, which was derived for uniform inflow, to the ABL inflows in this work, where U_{REWS} is the streamwise velocity upstream (which may include wakes from leading turbines) averaged over the rotor extent. The shear layer growth rate is $\beta = 0.1403$ (Liew et al., 2024). The nonlinear pressure field $p(x, y)$ as a function of streamwise x and spanwise y directions is computed with a fast, two-dimensional convolution between the nonlinear advective terms, and the nonlinear wake pressure $p^{\mathrm{NL}}(C_T', \gamma, a_n, x_0)$ is sampled at the location $p(x_0, 0)$ (full details in Liew et al., 2024). The near-wake length model derived in section 3.3.1, used to separate the near- and far-wake region in the TANDEM model, is computed separately from the iterative solution for the UMM rotor quantities using the UMM outputs u_4 and a_n.

https://doi.org/10.5194/wes-2026-149
Preprint. Discussion started: 27 August 2026

Wind Energy Science Discussions

Appendix C: Derivation of the momentum-corrected initial deficit radius

We seek a smoothed top-hat wake initial condition, stamped at $x = 0$ with radius R_d and depth δu_0, such that after the wake diffuses to the near-wake length $x = x_0$, the momentum integral (eq. (28)) matches the turbine thrust:

$$M(x_0) \equiv \iint (\overline{u^B} + \overline{\Delta u})\,\overline{\Delta u}\,dA\Big|_{x_0} = -F_T\cos(\gamma)/\rho, \tag{C1}$$

where u^B is the base ABL flow. For the uniform inflow case treated below, $u^B = u_\infty$.

Following Ali et al. (2024, Appendix B), the momentum integral of a top-hat deficit of radius R_d and depth $\delta u_0 < 0$, after spreading to the diffusion length scale σ, has the closed form

$$M(\sigma; R_d) = \underbrace{\pi R_d^2\,\delta u_0\,u_\infty}_{A_1} + \underbrace{\pi R_d^2\,\frac{\delta u_0^2}{2}\,\Lambda(\sigma/R_d)}_{A_2}, \tag{C2}$$

where $\Lambda(\sigma/R_d)$ is approximated by (Ali et al., 2024, eq. B21):

$$\Lambda(\sigma/R_d) = 2\left(\mathrm{erf}\left(\frac{R_d}{\sigma}\right) - \frac{\sigma}{R_d\sqrt{\pi}}\left(1 - \exp(-R_d^2/\sigma^2)\right)\right)^2. \tag{C3}$$

Λ is a monotonically decreasing function with $\Lambda(0) = 2$ (corresponding to a sharp top-hat) and $\Lambda(\sigma/R_d) \to 0$ as $\sigma/R_d \to \infty$ and the wake is fully diffused. Term A_1 is conserved under σ in the linear diffusion model of Ali et al. (2024). Term A_2 shrinks monotonically with σ: as the deficit spreads into the surrounding higher-velocity flow, the quadratic term dilutes. Because $\delta u_0 < 0$ and Term A_1 is fixed while Term A_2 (positive) shrinks, M becomes increasingly negative as σ grows.

We want to solve for R_d, given σ_{IC}, such that the following condition at $x = x_0$ is satisfied:

$$M(\sigma_0; R_d) = -F_T\cos(\gamma)/\rho \tag{C4}$$

To make the σ_{IC}-evaluated solve enforce $M(x_0) = -F_T\cos(\gamma)/\rho$, define the correction factor

$$\eta(R_d) \equiv \frac{M(\sigma_{\mathrm{IC}}; R_d)}{M(\sigma_0; R_d)} = \frac{u_\infty + \frac{1}{2}\delta u_0\,\Lambda(\sigma_{\mathrm{IC}}/R_d)}{u_\infty + \frac{1}{2}\delta u_0\,\Lambda(\sigma_0/R_d)}, \tag{C5}$$

using eq. (C2) for the numerator and denominator. Upon substituting $M(\sigma_0; R_d) = M(\sigma_{\mathrm{IC}}; R_d)/\eta$ into eq. (C4) and rearranging, we arrive at an implicit equation for R_d which can be solved iteratively:

$$M(\sigma_{\mathrm{IC}}; R_d) = -\frac{F_T\cos(\gamma)}{\rho}\,\eta(R_d). \tag{C6}$$

Specifically, finding R_d to satisfy eq. (C6) also results in satisfying eq. (C4). Picking the near-wake length x_0 as the matching location is convenient because at $x = x_0$, the wake is transitioning to the onset of the Gaussian wake. Fitting σ_0 to a wake at $x = x_0$ yields $\sigma_0 = 0.21D$. Therefore, σ_0 is known and, given σ_{IC}, which should be chosen to be as small as possible while avoiding numerical instabilities, one can compute the correction factor $\eta(R_d)$. We find that $\sigma_{\mathrm{IC}} = h/2$ works well, where h is the average grid size in the y and z directions.

Equation (C6) is nonlinear in R_d, since $\Lambda(\sigma_0/R_d)$ depends on R_d and can be solved by fixed-point iteration:

https://doi.org/10.5194/wes-2026-149
Preprint. Discussion started: 27 August 2026

1. Begin with an initial guess $R_d = R$
2. Build the Gaussian-smoothed top-hat stencil of radius R_d given smoothing width σ_{IC}.
3. Numerically integrate $M_{\text{numerical}}(\sigma_{\mathrm{IC}}; R_d)$ on the grid.
4. Compare against the target eq. (C6) (evaluated using the current guess of R_d); update R_d; repeat steps 2–4 to convergence.

The converged value is $R_d^{\text{corr}} \equiv R_d(C_T'; \sigma_{\mathrm{IC}})$, shown in fig. 5($b$,$c$).

Author contributions. K.S.H. and M.F.H. conceived the research. K.S.H. developed the model code, performed the LES, and analyzed the data. Both authors contributed to writing and editing the manuscript.

Competing interests. The authors declare no competing interests.

Acknowledgements. K.S.H. and M.F.H. gratefully acknowledge funding from the National Science Foundation (grant number 2542240). K.S.H. acknowledges additional funding through a National Science Foundation Graduate Research Fellowship under grant number DGE-2141064. Simulations and postprocessing were performed on the Stampede3 supercomputer under the NSF ACCESS project ATM170028.

Code and data availability. All of the data and code to generate the figures in this study are available at https://github.com/Howland-Lab/tandem_model. The TANDEM model is distributed through the open-source wind farm flow simulator MITWindfarm at https://github.com/Howland-Lab/MITWindfarm/. Large-eddy simulations were performed using PadéOps, which is available as open source at https://github.com/Howland-Lab/PadeOps. Full LES datasets used in this study may be available from the authors upon reasonable request.

https://doi.org/10.5194/wes-2026-149
Preprint. Discussion started: 27 August 2026

References

Abkar, M. and Porté-Agel, F.: Influence of Atmospheric Stability on Wind-Turbine Wakes: A Large-Eddy Simulation Study, Physics of Fluids, 27, 035 104, 2015.

Abkar, M. and Porté-Agel, F.: Influence of the Coriolis Force on the Structure and Evolution of Wind Turbine Wakes, Physical Review Fluids, 1, 063 701, 2016.

Abkar, M., Bae, H. J., and Moin, P.: Minimum-Dissipation Scalar Transport Model for Large-Eddy Simulation of Turbulent Flows, Physical Review Fluids, 1, 041 701, 2016.

Abkar, M., Sørensen, J. N., and Porté-Agel, F.: An Analytical Model for the Effect of Vertical Wind Veer on Wind Turbine Wakes, Energies, 11, 1838, 2018.

Aerts, F., Devesse, K., and Meyers, J.: Bayesian Uncertainty Quantification of Engineering Models for Wind Farm–Atmosphere Interaction, Wind Energy Science, 11, 1205–1225, 2026.

Ainslie, J. F.: Calculating the Flowfield in the Wake of Wind Turbines, Journal of Wind Engineering and Industrial Aerodynamics, 27, 213–224, 1988.

Ali, K., Stallard, T., and Ouro, P.: A Diffusion-Based Wind Turbine Wake Model, Journal of Fluid Mechanics, 1001, A13, 2024.

Bastankhah, M. and Porté-Agel, F.: A New Analytical Model for Wind-Turbine Wakes, Renewable Energy, 70, 116–123, 2014.

Bastankhah, M. and Porté-Agel, F.: Experimental and Theoretical Study of Wind Turbine Wakes in Yawed Conditions, Journal of Fluid Mechanics, 806, 506–541, 2016.

Bastankhah, M., Shapiro, C. R., Shamsoddin, S., Gayme, D. F., and Meneveau, C.: A Vortex Sheet Based Analytical Model of the Curled Wake behind Yawed Wind Turbines, Journal of Fluid Mechanics, 933, A2, 2022.

Bastankhah, M., Zunder, J. K., Hydon, P. E., Deebank, C., and Placidi, M.: Modelling Turbulence in Axisymmetric Wakes: An Application to Wind Turbine Wakes, Journal of Fluid Mechanics, 1000, A2, 2024.

Bay, C. J., Fleming, P., Doekemeijer, B., King, J., Churchfield, M., and Mudafort, R.: Addressing Deep Array Effects and Impacts to Wake Steering with the Cumulative-Curl Wake Model, Wind Energy Science, 8, 401–419, 2023.

Blackadar, A. K.: The Vertical Distribution of Wind and Turbulent Exchange in a Neutral Atmosphere, Journal of Geophysical Research (1896-1977), 67, 3095–3102, 1962.

Bogacki, P. and Shampine, L. F.: A 3(2) Pair of Runge - Kutta Formulas, Applied Mathematics Letters, 2, 321–325, 1989.

Bourhis, M., Messmer, T., Hölling, M., and Buxton, O.: Impact of Free-Stream Turbulence and Thrust Coefficient on Wind Turbine-Generated Wakes, Journal of Fluid Mechanics, 1023, A3, 2025.

Bromm, M., Vollmer, L., and Kühn, M.: Numerical Investigation of Wind Turbine Wake Development in Directionally Sheared Inflow, Wind Energy, 20, 381–395, 2017.

Brutsaert, W.: Mean Profiles and Similarity in a Stationary and Horizontally-Uniform ABL, in: Evaporation into the Atmosphere: Theory, History and Applications, edited by Brutsaert, W., pp. 57–112, Springer Netherlands, Dordrecht, ISBN 978-94-017-1497-6, 1982.

Burton, T., Jenkins, N., Sharpe, D., and Bossanyi, E.: Wind Energy Handbook, John Wiley & Sons, ISBN 978-1-119-99392-6, 2011.

Calaf, M., Meneveau, C., and Meyers, J.: Large Eddy Simulation Study of Fully Developed Wind-Turbine Array Boundary Layers, Physics of Fluids, 22, 015 110, 2010.

Chamorro, L. P. and Porté-Agel, F.: Effects of Thermal Stability and Incoming Boundary-Layer Flow Characteristics on Wind-Turbine Wakes: A Wind-Tunnel Study, Boundary-Layer Meteorology, 136, 515–533, 2010.

https://doi.org/10.5194/wes-2026-149
Preprint. Discussion started: 27 August 2026

Churchfield, M. J. and Sirnivas, S.: On the Effects of Wind Turbine Wake Skew Caused by Wind Veer, in: 2018 Wind Energy Symposium, American Institute of Aeronautics and Astronautics, Kissimmee, Florida, ISBN 978-1-62410-522-7, 2018.

Crespo, A. and Hernández, J.: Turbulence Characteristics in Wind-Turbine Wakes, Journal of Wind Engineering and Industrial Aerodynamics, 61, 71–85, 1996.

Du, B., Ge, M., Zeng, C., Cui, G., and Liu, Y.: Influence of Atmospheric Stability on Wind-Turbine Wakes with a Certain Hub-Height Turbulence Intensity, Physics of Fluids, 33, 055 111, 2021.

Frandsen, S., Barthelmie, R., Pryor, S., Rathmann, O., Larsen, S., Højstrup, J., and Thøgersen, M.: Analytical Modelling of Wind Speed Deficit in Large Offshore Wind Farms, Wind Energy, 9, 39–53, 2006.

Gaertner, E., Rinker, J., Sethuraman, L., Zahle, F., Anderson, B., Barter, G., Abbas, N., Meng, F., Bortolotti, P., Skrzypinski, W., Scott, G., Feil, R., Bredmose, H., Dykes, K., Shields, M., Allen, C., and Viselli, A.: Definition of the IEA 15-Megawatt Offshore Reference Wind Turbine, Tech. Rep. NREL/TP-5000-75698, National Renewable Energy Lab (NREL), Golden, CO, United States, 2020.

Gambuzza, S. and Ganapathisubramani, B.: The Influence of Free Stream Turbulence on the Development of a Wind Turbine Wake, Journal of Fluid Mechanics, 963, A19, 2023.

Gebraad, P. M. O., Teeuwisse, F. W., van Wingerden, J. W., Fleming, P. A., Ruben, S. D., Marden, J. R., and Pao, L. Y.: Wind Plant Power Optimization through Yaw Control Using a Parametric Model for Wake Effects—a CFD Simulation Study, Wind Energy, 19, 95–114, 2016.

Ghate, A. S. and Lele, S. K.: Subfilter-Scale Enrichment of Planetary Boundary Layer Large Eddy Simulation Using Discrete Fourier–Gabor Modes, Journal of Fluid Mechanics, 819, 494–539, 2017.

Ghate, A. S., Ghaisas, N., Lele, S. K., and Towne, A.: Interaction of Small Scale Homogenous Isotropic Turbulence with an Actuator Disk, in: 2018 Wind Energy Symposium, American Institute of Aeronautics and Astronautics, Kissimmee, Florida, ISBN 978-1-62410-522-7, 2018.

Glauert, H.: The Analysis of Experimental Results in the Windmill Brake and Vortex Ring States of an Airscrew, Tech. Rep. 177582, Royal Aircraft Establishment, Farnborough, 1926.

Gottlieb, S., Ketcheson, D., and Shu, C.-W.: Strong Stability Preserving Runge-Kutta and Multistep Time Discretizations, Wspc, Hackensack, NJ, 1st edition edn., ISBN 978-981-4289-26-9, 2011.

Gribben, B. J. and Hawkes, G. S.: A Potential Flow Model for Wind Turbine Induction and Wind Farm Blockage, Tech. rep., Frazer-Nash Consultancy, 2019.

Guilloré, A., Campagnolo, F., and Bottasso, C. L.: A Control-Oriented Load Surrogate Model Based on Sector-Averaged Inflow Quantities: Capturing Damage for Unwaked, Waked, Wake-Steering and Curtailed Wind Turbines, Journal of Physics: Conference Series, 2767, 032 019, 2024.

Heck, K. S. and Howland, M. F.: Coriolis Effects on Wind Turbine Wakes across Neutral Atmospheric Boundary Layer Regimes, Journal of Fluid Mechanics, 1008, A7, 2025.

Heck, K. S. and Howland, M. F.: Unravelling the Effects of Atmospheric Dynamics on Wakes with a Controlled Synthetic Inflow Methodology, Flow, 6, E24, 2026.

Heck, K. S., Liew, J., and Howland, M. F.: Investigation of Far-Wake Models Coupled with Yaw-Induction Control for Power Optimization, Journal of Physics: Conference Series, 2767, 092 103, 2024.

Heck, K. S., Liew, J., Upfal, I. M. L., and Howland, M. F.: Joint Yaw-Induction Control Optimization for Wind Farms, Wind Energy Science Discussions, pp. 1–40, 2025.

https://doi.org/10.5194/wes-2026-149
Preprint. Discussion started: 27 August 2026

Heck, K. S., Mata, S. A., and Howland, M. F.: Influence of Wind Shear and Veer on Power, Thrust, and Induction of an Actuator Disk, 2026.

Hodgson, E. L., Madsen, M. H. A., and Andersen, S. J.: Effects of Turbulent Inflow Time Scales on Wind Turbine Wake Behavior and Recovery, Physics of Fluids, 35, 095 125, 2023.

Howland, M. F., Bossuyt, J., Martínez-Tossas, L. A., Meyers, J., and Meneveau, C.: Wake Structure in Actuator Disk Models of Wind Turbines in Yaw under Uniform Inflow Conditions, Journal of Renewable and Sustainable Energy, 8, 043 301, 2016.

Howland, M. F., Ghate, A. S., and Lele, S. K.: Influence of the Geostrophic Wind Direction on the Atmospheric Boundary Layer Flow, Journal of Fluid Mechanics, 883, A39, 2020.

Ishihara, T. and Qian, G.-W.: A New Gaussian-based Analytical Wake Model for Wind Turbines Considering Ambient Turbulence Intensities and Thrust Coefficient Effects, Journal of Wind Engineering and Industrial Aerodynamics, 177, 275–292, 2018.

Iungo, G. V., Santhanagopalan, V., Ciri, U., Viola, F., Zhan, L., Rotea, M. A., and Leonardi, S.: Parabolic RANS Solver for Low-Computational-Cost Simulations of Wind Turbine Wakes, Wind Energy, 21, 184–197, 2018.

Jensen, N. O.: A Note on Wind Generator Interaction, Risø National Laboratory, Roskilde, Denmark, ISBN 978-87-550-0971-4, 1983.

Khanjari, A., Feroz, A., and Archer, C. L.: An Analytical Formulation for Turbulence Kinetic Energy Added by Wind Turbines Based on Large-Eddy Simulation, Wind Energy Science, 10, 887–905, 2025.

Kirby, A., Nishino, T., Lanzilao, L., Dunstan, T. D., and Meyers, J.: Turbine- and Farm-Scale Power Losses in Wind Farms: An Alternative to Wake and Farm Blockage Losses, Wind Energy Science, 10, 435–450, 2025.

Klemmer, K. S. and Howland, M. F.: Momentum Deficit and Wake-Added Turbulence Kinetic Energy Budgets in the Stratified Atmospheric Boundary Layer, Physical Review Fluids, 9, 114 607, 2024.

Klemmer, K. S. and Howland, M. F.: Wake Turbulence Modeling in Stratified Atmospheric Flows Using a Novel k–l Model, Journal of Renewable and Sustainable Energy, 17, 033 304, 2025.

Lanzilao, L. and Meyers, J.: A Parametric Large-Eddy Simulation Study of Wind-Farm Blockage and Gravity Waves in Conventionally Neutral Boundary Layers, Journal of Fluid Mechanics, 979, A54, 2024.

Lee, J. H. W. and Chu, V. H.: Turbulent Jets and Plumes, Springer US, Boston, MA, ISBN 978-1-4613-5061-3 978-1-4615-0407-8, 2003.

Liew, J., Urbán, A. M., and Andersen, S. J.: Analytical Model for the Power–Yaw Sensitivity of Wind Turbines Operating in Full Wake, Wind Energy Science, 5, 427–437, 2020.

Liew, J., Heck, K. S., and Howland, M. F.: Unified Momentum Model for Rotor Aerodynamics across Operating Regimes, Nature Communications, 15, 1–12, 2024.

Lissaman, P. B. S.: Energy Effectiveness of Arbitrary Arrays of Wind Turbines, Journal of Energy, 3, 323–328, 1979.

Liu, L., Gadde, S. N., and Stevens, R. J.: Geostrophic Drag Law for Conventionally Neutral Atmospheric Boundary Layers Revisited, Quarterly Journal of the Royal Meteorological Society, 147, 847–857, 2021.

Lopez-Gomez, I., Cohen, Y., He, J., Jaruga, A., and Schneider, T.: A Generalized Mixing Length Closure for Eddy-Diffusivity Mass-Flux Schemes of Turbulence and Convection, Journal of Advances in Modeling Earth Systems, 12, e2020MS002 161, 2020.

Madsen, H. A., Larsen, T. J., Pirrung, G. R., Li, A., and Zahle, F.: Implementation of the Blade Element Momentum Model on a Polar Grid and Its Aeroelastic Load Impact, Wind Energy Science, 5, 1–27, 2020.

Mahrt, L.: Stably Stratified Atmospheric Boundary Layers, Annual Review of Fluid Mechanics, 46, 23–45, 2014.

Martínez-Tossas, L. A., Annoni, J., Fleming, P. A., and Churchfield, M. J.: The Aerodynamics of the Curled Wake: A Simplified Model in View of Flow Control, Wind Energy Science, 4, 127–138, 2019.

Martínez-Tossas, L. A., King, J., Quon, E., Bay, C. J., Mudafort, R., Hamilton, N., Howland, M. F., and Fleming, P. A.: The Curled Wake Model: A Three-Dimensional and Extremely Fast Steady-State Wake Solver for Wind Plant Flows, Wind Energy Science, 6, 555–570, 2021.

Martínez-Tossas, L. A., Branlard, E., Shaler, K., Vijayakumar, G., Ananthan, S., Sakievich, P., and Jonkman, J.: Numerical Investigation of Wind Turbine Wakes under High Thrust Coefficient, Wind Energy, 25, 605–617, 2022.

Meyers, J., Bottasso, C., Dykes, K., Fleming, P., Gebraad, P., Giebel, G., Göçmen, T., and van Wingerden, J.-W.: Wind Farm Flow Control: Prospects and Challenges, Wind Energy Science, 7, 2271–2306, 2022.

Mohammadi, M., Bastankhah, M., Fleming, P., Churchfield, M., Bossanyi, E., Landberg, L., and Ruisi, R.: Curled-Skewed Wakes behind Yawed Wind Turbines Subject to Veered Inflow, Energies, 15, 9135, 2022.

Nagarajan, S., Lele, S. K., and Ferziger, J. H.: A Robust High-Order Compact Method for Large Eddy Simulation, Journal of Computational Physics, 191, 392–419, 2003.

Narasimhan, G., Gayme, D. F., and Meneveau, C.: Effects of Wind Veer on a Yawed Wind Turbine Wake in Atmospheric Boundary Layer Flow, Physical Review Fluids, 7, 114 609, 2022.

Narasimhan, G., Gayme, D. F., and Meneveau, C.: An Extended Analytical Wake Model and Applications to Yawed Wind Turbines in Atmospheric Boundary Layers with Different Levels of Stratification and Veer, Journal of Renewable and Sustainable Energy, 17, 033 302, 2025.

Niayifar, A. and Porté-Agel, F.: Analytical Modeling of Wind Farms: A New Approach for Power Prediction, Energies, 9, 741, 2016.

Nicoud, F., Toda, H. B., Cabrit, O., Bose, S., and Lee, J.: Using Singular Values to Build a Subgrid-Scale Model for Large Eddy Simulations, Physics of Fluids, 23, 085 106, 2011.

Nordström, J., Nordin, N., and Henningson, D.: The Fringe Region Technique and the Fourier Method Used in the Direct Numerical Simulation of Spatially Evolving Viscous Flows, SIAM Journal on Scientific Computing, 20, 1365–1393, 1999.

Pedersen, J. G., Svensson, E., Poulsen, L., and Nygaard, N. G.: Turbulence Optimized Park Model with Gaussian Wake Profile, Journal of Physics: Conference Series, 2265, 022 063, 2022.

Peña, A., Réthoré, P.-E., and van der Laan, M. P.: On the Application of the Jensen Wake Model Using a Turbulence-Dependent Wake Decay Coefficient: The Sexbierum Case, Wind Energy, 19, 763–776, 2016.

Porté-Agel, F., Bastankhah, M., and Shamsoddin, S.: Wind-Turbine and Wind-Farm Flows: A Review, Boundary-Layer Meteorology, 174, 1–59, 2020.

Qian, G.-W. and Ishihara, T.: A New Analytical Wake Model for Yawed Wind Turbines, Energies, 11, 665, 2018.

Revaz, T. and Porté-Agel, F.: Effect of Turbulence Intensity on the Induction Factor and Power Efficiency of Wind Turbines, Wind Energy, 28, e70 040, 2025.

Sanchez Gomez, M., Lundquist, J. K., Mirocha, J. D., and Arthur, R. S.: Investigating the Physical Mechanisms That Modify Wind Plant Blockage in Stable Boundary Layers, Wind Energy Science, 8, 1049–1069, 2023.

Scott, R., Martínez-Tossas, L., Bossuyt, J., Hamilton, N., and Cal, R. B.: Evolution of Eddy Viscosity in the Wake of a Wind Turbine, Wind Energy Science, 8, 449–463, 2023.

Shapiro, C. R., Gayme, D. F., and Meneveau, C.: Filtered Actuator Disks: Theory and Application to Wind Turbine Models in Large Eddy Simulation, Wind Energy, 22, 1414–1420, 2019.

Shapiro, C. R., Gayme, D. F., and Meneveau, C.: Generation and Decay of Counter-Rotating Vortices Downstream of Yawed Wind Turbines in the Atmospheric Boundary Layer, Journal of Fluid Mechanics, 903, R2, 2020.

https://doi.org/10.5194/wes-2026-149
Preprint. Discussion started: 27 August 2026

Shen, Z., Liu, L., Lu, X., and Stevens, R. J. A. M.: The Global Properties of Nocturnal Stable Atmospheric Boundary Layers, Journal of Fluid Mechanics, 999, A60, 2024.

Stevens, R. J., Graham, J., and Meneveau, C.: A Concurrent Precursor Inflow Method for Large Eddy Simulations and Applications to Finite Length Wind Farms, Renewable Energy, 68, 46–50, 2014.

Stevens, R. J. A. M. and Meneveau, C.: Flow Structure and Turbulence in Wind Farms, Annual Review of Fluid Mechanics, 49, 311–339, 2017.

Stevens, R. J. A. M., Gayme, D. F., and Meneveau, C.: Generalized Coupled Wake Boundary Layer Model: Applications and Comparisons with Field and LES Data for Two Wind Farms, Wind Energy, 19, 2023–2040, 2016.

Tennekes, H. and Lumley, J. L.: A First Course in Turbulence, MIT Press, Cambridge, Mass, ISBN 978-0-262-20019-6, 1972.

Vahidi, D. and Porté-Agel, F.: Influence of Incoming Turbulent Scales on the Wind Turbine Wake: A Large-Eddy Simulation Study, Physics of Fluids, 36, 095 177, 2024.

van der Laan, M. P. and Sørensen, N. N.: Why the Coriolis Force Turns a Wind Farm Wake Clockwise in the Northern Hemisphere, Wind Energy Science, 2, 285–294, 2017.

van der Laan, M. P., Kelly, M., Baungaard, M., Dicholkar, A., and Hodgson, E. L.: A Simple Steady-State Inflow Model of the Neutral and Stable Atmospheric Boundary Layer Applied to Wind Turbine Wake Simulations, Wind Energy Science, 9, 1985–2000, 2024.

Wu, S., Archer, C. L., and Mirocha, J. D.: New Insights on Wind Turbine Wakes from Large-Eddy Simulation: Wake Contraction, Dual Nature, and Temperature Effects, Wind Energy, 27, 1130–1151, 2024.

Wu, Y.-T. and Porté-Agel, F.: Atmospheric Turbulence Effects on Wind-Turbine Wakes: An LES Study, Energies, 5, 5340–5362, 2012.

Xie, S. and Archer, C. L.: A Numerical Study of Wind-Turbine Wakes for Three Atmospheric Stability Conditions, Boundary-Layer Meteorology, 165, 87–112, 2017.